UNIVERSITY OF GHANA, LEGON

COLLEGE OF BASIC AND APPLIED SCIENCES

THE EFFECTS OF HARMATTAN DUST AND RAINFALL ON MICROWAVE SIGNALS IN PARTS OF GHANA

By

CHRISTINE AFIA ACHEAMPONG

(10327645)

THIS THESIS IS SUBMITTED TO THE UNIVERSITY
OF GHANA, LEGON, IN PARTIAL FULFILMENT OF
THE REQUIREMENT FOR THE AWARD OF
DOCTOR OF PHILOSOPHY IN PHYSICS DEGREE

JULY 2019

DECLARATION

I, Christine Afia Acheampong, hereby declare that except for the references to other peoples' works, which have been duly acknowledged, this thesis is the result of my own research work towards earning a Ph.D. as a student of the University of Ghana, Legon, under the supervision of the Supervisory Committee as detailed below:

……………………………………………………….. Date:

…………………………………………

CHRISTINE AFIA ACHEAMPONG
(Candidate)

……………………………………………………….. Date:

…………………………………………

DR. V. C. K. KAKANE
(Principal Supervisor)

……………………………………………………….. Date:

…………………………………………

PROF. J. K. A. AMUZU
(Supervisor)

ABSTRACT

Microwave signal attenuation due to harmattan and rainfall are two of the major constraints in selecting microwave bands in Ghana. With customer complaints of signal loss during these seasons, telecommunication companies compensate for sudden losses in signal strength by amplifying the signal wave. This study investigates the effect of harmattan and rainfall on communication link for frequencies ranging from 10 to 100 GHz for two locations in Ghana, namely Axim and Tamale.

Visibility and rain rate measurements were made over a two-year period in these locations (Axim and Tamale). The signal attenuation as a result of harmattan dust was calculated using the Zain Elabdin model for visibilities from measured data. The microwave attenuation was obtained for frequencies ranging from 10 GHz to 100 GHz. The rain attenuation was determined using the ITU-R Specific Attenuation Model for Rain (ITU-R P.838-3) for the design of microwave communication systems.

The results showed that both harmattan dust and rainfall have a significant impact on signal attenuation in parts of Ghana. The effect of attenuation due to harmattan dust was much more evident in Tamale whiles rain attenuation was more evident in Axim.

It was observed that the signal attenuation increased as the radius size increased for frequencies from 10 – 100 GHz.

The signal attenuation due to harmattan dust was calculated for frequencies ranging from 10 – 100 GHz for both Tamale and Axim. The signal attenuation due to harmattan dust increased with increasing frequencies for both locations. Upon comparison, it was observed that Tamale had the higher attenuation values. Axim showed relatively low attenuation values from frequencies of 10 GHz to 100 GHz and ranged from 0.00009 dB/km to 0.03841 dB/km whiles signal attenuation values for Tamale increased from 0.00146 dB/km to a maximum value of 0.6272 dB/km. This graph shows that attenuation due to dust was more prevalent in the Tamale than in Axim.

Furthermore, attenuation values calculated using measured rain rate were highest for high rainfall rates while the lowest attenuation values corresponded to the lowest rainfall rates, as shown in the ITU-R rain attenuation model.

DEDICATION

I dedicate this work to my Auslin, April, Paul, Joshua, Adriel and Aaron.

ACKNOWLEDGMENTS

First, I am deeply grateful to my supervisors, Dr. V. C. K. Kakane and Prof. J. K. A. Amuzu for their guidance, suggestions and encouragement throughout my research.

I am sincerely grateful to Dr. G. K. Nkrumah-Buandoh, Dr. Allison Felix Hughes, Dr. Hubert Azoda Koffi, Dr. Godfred Bright Hagan, Dr. Amos Kuditcher and Dr. M. N. Y. H. Egblewogbe who are all lecturers in the Department of Physics, University of Ghana, for the keen interest showed and the useful counsel they offered me.

I am also grateful to my colleagues in this PhD journey in the Department of Physics - Dr. Joanna A. Modupeh Hodasi, Dr. Kofi Ampomah Benefo and Mr.George Kusi-Appiah. We encouraged each other and we were our biggest fans. I am very grateful to Mr. Harry Ntumi, for all the technical insight and help, especially during the installation of all the equipment at the various test sites. I would also like to say thank you to Pamphile Tossou, Frederick Tatah and all the technicians for the technical support offered.

Finally, my heartfelt gratitude go to Mr. Julian Ebo Kennedy, Mr. David Kingsley Acheampong, Linda Acheampong, Olivia Acheampmong and Michael Acheampong for their prayers and warm support given to me all these years. God bless you all.

TABLE OF CONTENTS

DECLARATION i

ABSTRACT ii

DEDICATION iv

ACKNOWLEDGEMENTS v

TABLE OF CONTENTS vi

LIST OF FIGURES xi

LIST OF TABLES xi

ABBREVIATIONS xviii

CHAPTER ONE: THE PHYSICS OF RADIOWAVES AND THEIR PROPAGATION

1.1 Electromagnetic Theory 2

1.2 The Theory of EM Waves 4

1.2.1 The Electric Field 5

1.2.2 The Magnetic Field……… .. ……………………………………7

1.2.3 Maxwells Equations 12

1.3 Generation of Radiowaves 15

1.4 Propagation of Radiowaves 16

1.4.1 Atmospheric Propagation 19

1.4.1.1 Ionospheric Propagation 21

1.4.1.2 Tropospheric Propagation 23

1.5 Transmission of Radiowaves 24

1.5.1 Modulation 25

1.5.2 Amplification 27

1.5.3 Antennae 28

1.5.4 Transmission Systems 30

1.6 Scattering and Attenuation of EM Waves 31

1.6.1 Rain 32

1.6.2 Fog 32

1.6.3 Harmattan 33

1.7 Aim and Objectives of the Study 33

1.8 Justification e of the Study 34

1.9 Scope of the Study 35

1.10 General Form of the Thesis 36

CHAPTER TWO: STUDIES OF THE EFFECTS OF DUST, FOG AND RAIN ON RADIOWAVES

2.1 Climate of Ghana 38

2.2 Effects of Dust........ 49

2.3 Effects of Fog........ 50

2.4 Effects of Rain........ 51

CHAPTER THREE: THE RAYLEIGH AND MIE ATTENUATION MODELS FOR WAVES

3.1 Scattering And Absorption In The Atmosphere........ 55

3.1.1 Polarization of a Wave 56

3.2 Theory of Single Particle Scattering 56

3.3 Approximation Methods/Models for Scattering 59

3.3.2 Rayleigh Approximation 60

3.3.2 Mie Approximation........ 61

3.4 Signal Attenuation due to Harmattan Dust 63

3.4.1 Harmattan Dust Predicted Model 64

3.4.1.1 Using Rayleigh Approximation 65

3.4.1.2 Using Mie Approximation 65

3.4.2 Dependence on Visibility........ 66

3.4.4 Zain Elabdin Model 67

3.5 The ITU-R Rain Attenuation Model... 70

CHAPTER FOUR: STUDY SITES, EQUIPMENT AND DATA ACQUISITION

4.1 Study Sites.. 74

4.1.1 Axim Site 74

4.1.2 Tamale Site... 76

4.2 Equipment Used 78

4.2.1 Campbell Scientific CS120 Visibility Sensor 79

4.2.2 MiniOFS Optical Sensor 81

4.2.3 Davis Vantage Pro 2 Weather Station.. 82

4.2.4 Campbell Scientific CR1000 Datalogger..................................... 84

4.3 Methodology 86

4.4 Data Analysis 95

CHAPTER FIVE: RESULTS AND DISCUSSIONS

5.1 Signal Attenuation Analysis.. 97

5.2 Axim Measurements 98

5.2.1 Harmattan Dust Results... 98

5.2.1.1 Attenuation for the Different Frequency Bands........................ 98

5.2.2 Rain Rate Measurements.. 106

5.2.3 Additional Data Analysis (Axim) 108

5.3 Tamale Measurements 111

5.3.1 Harmattan Dust Results.. 111

5.3.2 Rain Rate Results 119

5.3.3 Additional Data Analysis (Tamale) 120

5.4 Signal Attenuation due to Dust for Different Radii 122

5.4.1 Comparison Between the Measured and Predicted Models........ 125

CHAPTER SIX: CONCLUSIONS AND RECOMMENDATION

6.1 Summary of Experiment 129

6.2 Key Results 129

6.2 Further Work and Recommendations 133

REFERENCES 135

LIST OF FIGURES

Figure 1.1: The Electromagnetic Spectrum..3

Figure 1.2: Electromagnetic Wave..5

Figure 1.3: Diagram showing a wire with steady line current, I and the vector from the source to the point, r 8

Figure 1.4: Diagram showing a long straight wire carrying a steady current, I 8

Figure 1.5: Magnetic Field due to current-carrying infinite wire 9

Figure 1.6: Line of Sight Propagation..17

Figure 1.7: Ground Wave Propagation 18

Figure 1.8: Sky Wave Propagation 19

Figure 1.9: Atmospheric Layers..20

Figure 1.10: Layers of the Ioonosphere over the period of a day 22

Figure 1.11: RadiowavesTransmission Media......................................25

Figure 2.1: Map of Ghana with its bordering countries 39

Figure 2.2: Climatic Zones in Ghana 41

Figure 2.3: Air masses and their source regions 43

Figure 2.4: Movements of the Inter-Tropical Convergence Zone and Rainfall 44

Figure 2.5: Mean Monthly Rainfall and Temperatures 48

Figure 3.1: Scattering Configuration 57

Figure 4.1: Map of Southern Ghana 75

Figure 4.2: Axim research site at the GMA office 76

Figure 4.3: : Map of Northern Part of Ghana 77

Figure 4.4: Tamale research site at the GMA office 78

Figure 4.5: Campbell Scientific CS120 Visibility Sensor 80

Figure 4.6: Mini OFS Optical Sensor 82

Figure 4.7: Vantage Pro 2 Integrated Sensor Suite (ISS) 83

Figure 4.8: Vantage Pro 2 Console 84

Figure 4.9: CR1000 Measurement and Control Datalogger 86

Figure 4.10: Setting the Transmitter ID for communication between the ISS and the console 87

Figure 4.11: Positioning the protective cage around the weather station at the Physics Department, University of Ghana 88

Figure 4.12: Complete ISS setup communicating with console 89

Figure 4.13: Setting up the Davis Vantage Pro 2 Weather Station at the Axim site 90

Figure 4.14: Installed Vantage Pro 2 Weather Station at the Tamale site 91

Figure 4.15: Concrete foundation for mount installation 92

Figure 4.16: Fully mounted visibility sensor 93

Figure 4.17: Set up of the CS120 Visibility Sensor and Vantage Pro 2 Weather Station at the Tamale site 94

Figure 5.1: Signal Attenuation versus Frequency at S-Band for Different Visibilities in Axim 100

Figure 5.2: Signal Attenuation versus Frequency at C-Band for Different Visibilities in Axim 100

Figure 5.3: Signal Attenuation versus Frequency at X-Band for Different Visibilities in Axim 101

Figure 5.4: Signal Attenuation versus Frequency at Ku-Band for Different Visibilities in Axim 101

Figure 5.5: Signal Attenuation versus Frequency at K-Band for Different Visibilities in Axim 102

Figure 5.6: Signal Attenuation versus Frequency at Ka-Band for Different Visibilities in Axim 102

Figure 5.7: Signal Attenuation versus Frequency at W-Band for Different Visibilities in Axim 103

Figure 5.8: Signal Attenuation due to harmattan against Frequency at Vis=3975.648936m for different radius sizes.....................................104

Figure 5.9: Signal Attenuation due to harmattan against Frequency at Vis=3995.711m for different radius sizes...104

Figure 5.10: Signal Attenuation due to harmattan against Frequency at Vis=4012.3935m for different radius sizes..105

Figure 5.11: Signal Attenuation due to harmattan against Frequency at Vis=4016.027m for different radius sizes...105

Figure 5.12: Graph of Rain Attenuation versus Frequency from August - December 2015 107

Figure 5.13: Graph of Rain Attenuation versus Frequency from January - April 2016 107

Figure 5.14: Graph of Visibility versus Rain Rate in Axim 109

Figure 5.15: Graph of Visibility versus Relative Humidity (All-Day, All weather) in Axim 110

Figure 5.16a: XYZ Graph of Visibility against Relative Humidity and Temperature 111

Figure 5.16b: XYZ Graph of Temperature against Visibility and Relative Humidity 111

Figure 5.17: Signal Attenuation versus Frequency at S-Band for Different Visibilities in Tamale 112

Figure 5.18: Signal Attenuation versus Frequency at C-Band for Different Visibilities in Tamale 113

Figure 5.19: Signal Attenuation versus Frequency at X-Band for Different Visibilities in Tamale 113

Figure 5.20: Signal Attenuation versus Frequency at Ku-Band for Different Visibilities in Tamale......114

Figure 5.21: Signal Attenuation versus Frequency at K-Band for Different Visibilities in Tamale 114

Figure 5.22: Signal Attenuation versus Frequency at Ka-Band for Different Visibilities in Tamale......115

Figure 5.23: Signal Attenuation versus Frequency at W-Band for Different Visibilities in Tamale......115

Figure 5.24: Signal Attenuation due to harmattan against Frequency at Vis=225.482m for different radii 117

Figure 5.25: Signal Attenuation due to harmattan against Frequency at Vis=232.64m for different radii 117

Figure 5.26: Signal Attenuation due to harmattan against Frequency at Vis=256.95m for different radii 118

Figure 5.27: Signal Attenuation due to harmattan against Frequency at Vis=261.70m for different radii 118

Figure 5.28: Graph of Rain Attenuation versus Frequency from April - June 2016...120

Figure 5.29: Graph of Visibility versus Relative Humidity (All-Day, All weather) in Tamale 121

Figure 5.30a: XYZ Graph of Visibility against Relative Humidity and Temperature 122

Figure 5.30b: XYZ Graph of Temperature against Visibility and Relative Humidity 122

Figure 5.31: Signal Attenuation due to harmattan against Visibility at 40GHz for different radii in Tamale 123

Figure 5.32: Signal Attenuation due to harmattan against Visibility at 40GHz for different radii in Axim 124

Figure 5.33: Result of Measurements and Calculations of Signal Attenuation due to harmattan at 40GHz...126

Figure 5.34: Comparison of Calculated Signal Attenuation due to harmattan dust at Different frequencies in Axim and Tamale 127

LIST OF TABLES

Table 1.1: Electromagnetic Spectrum and their Frequency Bands 4

Table 1.2: Basic Equations for Maxwell’s Equations 13

Table 1.3: Frequency Band Designations 15

Table 5.1: Dielectric constants for the different microwave frequency bands..99

Table 5.2: Result of Measurements and Calculations of Signal Attenuation Due To Harmattan at 40 GHz in Axim 125

LIST OF ABBREVIATIONS

VHF	Very high frequency
UHF	Ultra high frequency
AM	Amplitude Modulation
FM	Frequency Modulation
PM	Phase Modulation
RF	Radio frequency
RSL	Receive Signal Level
ITCZ	Inter Tropical Convergence Zone
ITU-R	International Communications Union Radiocommunication
CD	Cumulative distribution
LOS	Line-of-sight
VSAT	Very Small Aperture Terminal
PMMA	Polymethyl methacrylate
ISS	Integrated Sensor Suite

CHAPTER 1

THE PHYSICS OF RADIOWAVES AND THEIR PROPAGATION

Radio waves are one of the parts that comprises an electromagnetic radiation. They have the longest wavelength and the shortest frequencies. Other types of the electromagnetic radiation are visible light, microwaves,
infrared (IR), ultraviolet (UV), gamma-rays and X-rays. Radio waves are commonly used for communication; radio, television, cellphones etc.

Changing electric and magnetic fields constitute an electromagnetic radiation. At every point along the wave there is an electric field coupled with a magnetic field. The electric field is at right angle to the magnetic field.

A wave has properties such as speed, wavelength, and frequency. These are related by a simple expression ($\text{Speed} = \text{Frequency} \times \text{Wavelength}$). For electromagnetic waves, the speed is denoted by c (the speed of light). The speed of light in vacuum is $3 \times 10^{8}\ \text{m/s}$ and $c = f \times \lambda$. Electromagnetic waves unlike mechanical waves, do not need a medium in which to propagate but they can propagate through vacuum.

The wavelength (λ) is the distance measured from a point on one wave to the equivalent part of the next, for example from the top of one peak to the next. The frequency is the number of whole waves that pass a fixed point in a period of time. The speed has units in meters/second, whiles frequency has its units in cycles per second (or Hertz, abbreviated Hz), and wavelength is measured in meters.

Radio propagation talks about how radio waves travel, or are propagated from one point to another. Radio waves, like other types of EM radiation, are affected by the occurrences of reflection, refraction, diffraction, absorption, polarization, and scattering etc. There will be more in-depth information in the chapter.

Electromagnetic signals are transmitted in two ways: through a guided medium or through an unguided medium. Guided media such as coaxial and fiber optic cables have fewer challenges than the wireless or the unguided channel such as the atmosphere. As a signal travels through the wireless conduit, it goes through the influence of various kinds of propagation such as reflection, diffraction and scattering, due to the presence of buildings, mountains and other such obstructions (Mark, 2005).

1.1 ELECTROMAGNETIC THEORY

Wireless communications utilize electromagnetic waves in transferring signals across long distances. Electromagnetic waves are made up of an electric field coupled with a magnetic field. Electromagnetic waves do not need a medium to propagate. Hence, they can travel through vacuum. Electromagnetic waves extend over a wide range of frequencies. The frequency of an electromagnetic wave determines its characteristics. The EM wave spectrum is shown in Figure 1.1.

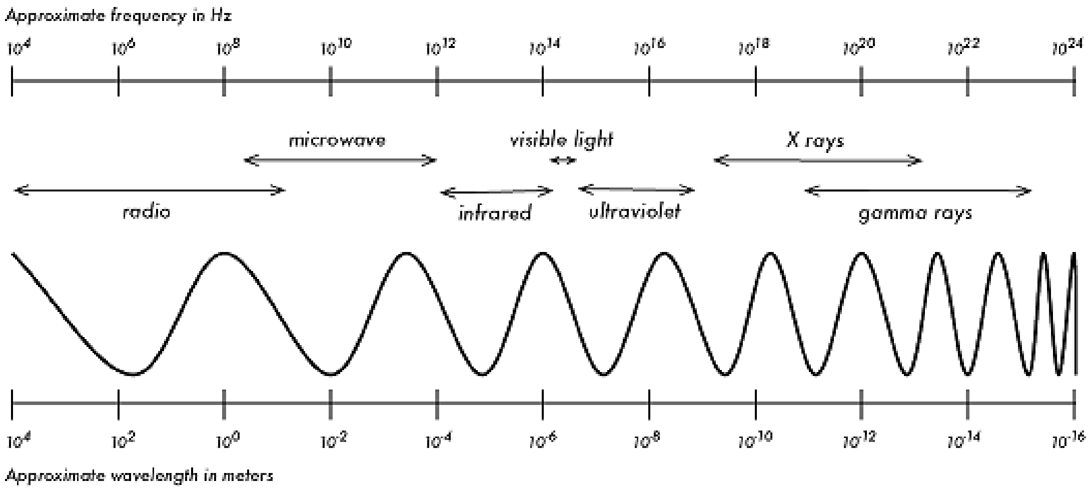

Figure 1.1: The Electromagnetic Spectrum

The electromagnetic spectrum is divided into different frequency bands as shown in Table 1.1.

Frequency Band	Frequency (Hz)	Wavelength	Use
Long wave, TV	$< 3 \times 10^{9}$ Hz	10^{5} to 10^{2} m	TV broadcast
Short Wave Radio	10^{8} to 3×10^{9} Hz	10^{2} to 10^{-1} m	AM and FM radio, Communication
Microwave	3×10^{9} to 3×10^{12} Hz	10^{-1} to 10^{-3} m	Cell phones, Wireless data, Microwaves, Satellites
Infrared	3×10^{12} to 4.3×10^{14} Hz	10^{-3} to 7×10^{-7} m	Remote Controls, Night Vision Lighting
Visible	4.3×10^{14} to 7.5×10^{14} Hz	7×10^{-7} to 4×10^{-7} m	Vision, Photography
Ultraviolet	7.5×10^{14} to 3×10^{17} Hz	4×10^{-7} to 10^{-9} m	Sun-tan lamps, Dental curing, Vitamin D source
X-Rays	3×10^{17} to 3×10^{19} Hz	10^{-9} to 10^{-11} m	Baggage Screening, Imaging bone defects
Gamma Rays	3×10^{19} to 10^{20} Hz	10^{-11} to 10^{-15} m	Cancer Treatment
Cosmic Rays	10^{20} to 10^{22} Hz	10^{-15} to 10^{-20} m	

Table 1.1: Electromagnetic Spectrum and their Frequency Bands

1.2 THE THEORY OF EM WAVES

Electromagnetic waves have two orthogonal time-varying fields: electric and magnetic components that oscillate simultaneously. The planes of the electric and magnetic fields are perpendicular to each other and also perpendicular to the direction of the wave propagation (Seybold, 2005, Griffiths, 1999).

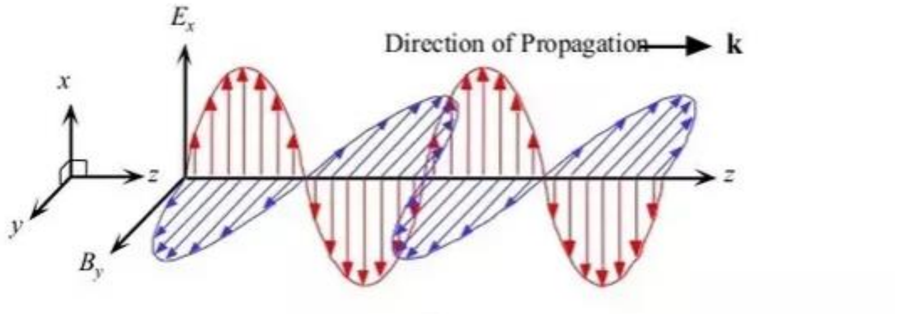

Figure 1.2: Electromagnetic Wave

1.2.1 The Electric Field

The electric field is defined as the vector force per unit charge. It is generated by an electric charge and is usually denoted by the symbol ***E***. The electric field is a vector quantity that varies from point to point. The unit of the electric field is Newtons per coulomb ($1\, N/C = 1\ V/m$).

The electric field (electrostatic field), ***E*** produced as a result of several point source point charges at distances $r_{1,}\ r_{2,}\ r_{3,}\ \ldots\ldots\ldots\ldots\ r_n$ from a test charge, Q, is given by

$$\vec{E} = \frac{\vec{F}}{Q} = \frac{1}{4\pi\varepsilon_o}\sum_{i=1}^{n}\frac{q_i}{{r_i}^2}\hat{r} \tag{1.1}$$

where Q is the test charge (assuming that Q is small), q_i is the stationary point charges, r_i is the distances between the point charges, q_i and the test charge, Q, F is the total electric force exerted by the point charges, q_i on the test charge, Q and ε_o is the permittivity in vacuum/free space

In more realistic conditions, the point (source) charges are usually continuous over a region and not discrete. Consequently, the E for continuous charges over a region becomes

$$\vec{E} = \frac{\vec{F}}{Q} = \frac{1}{4\pi\varepsilon_o}\int \frac{1}{r^2}\hat{r}\, dq \tag{1.2}$$

The three main distributions used are the line charge (λ), surface charge (σ) and volume charge (ρ). The flux of electric field lines through any surface is a measure of the number of field lines passing through the surface. Considering a point charge q at the origin, the electric flux, Φ_E through a closed surface, for example a sphere of radius r, centered on the origin, is equal to

$$\Phi_E = \oint \vec{E}.d\vec{A} = \frac{1}{4\pi\varepsilon_o}\int \left(\frac{q}{r^2}\hat{r}\right).(r^2 \sin\theta\, d\theta\, d\phi\, \hat{r}\,) = \frac{q}{\varepsilon_o} \tag{1.3}$$

Hence, for any arbitrary closed surface with any charge distribution, the electric flux Φ_E is given by

$$\oint \vec{E}.d\vec{A} = \frac{Q_{enc}}{\varepsilon_o} \tag{1.4}$$

where Q_{enc} is the total charge enclosed by the surface.

This is the integral form of the Gauss' Law (known as Gauss's law in integral form). Applying the divergence theorem, the differential form of the Gauss' Law can be written as: $\Phi_E = \oint_S \vec{E}.d\vec{A} = \int_V (\vec{\nabla}\cdot\vec{E})\, d\tau$

Therefore, equation 1.4 becomes

$$\int_V (\vec{\nabla}\cdot\vec{E})\, d\tau = \frac{1}{\varepsilon_o}\int_V \rho d\tau \tag{1.5}$$

Since this equation holds for any volume, the integrands will be equal and hence

$$\vec{\nabla} \cdot \vec{E} = \frac{\rho}{\varepsilon_o} \tag{1.6}$$

Equation 1.6 is known as Gauss's law in differential form.

Additionally, taking the line integral from some point a to another point b gives $\int_a^b E \cdot dl$

But $\vec{A} = dr\hat{r} + rd\theta\hat{\theta} + r\sin\theta\, d\phi\hat{\phi}$.

Therefore, $\vec{E} \cdot dl = \frac{1}{4\pi\varepsilon_o}\frac{q}{r^2}dr = \int_a^b E \cdot dl = \frac{1}{4\pi\varepsilon_o}\int_a^b \frac{q}{r^2}dr = \frac{1}{4\pi\varepsilon_o}(r_b - r_a)$

r_a is the distance from the starting point to point, a

r_b is the distance from the starting point to point b.

For a closed path, the integral will be zero since $r_b = r_a$. Therefore, $\oint \vec{E} \cdot dl = o$. Applying Stoke's theorem (curl of ***E***) to equation 1.6 gives

$$\vec{\nabla} \times \vec{E} = 0 \tag{1.7}$$

1.2.2 The Magnetic Field

Electric currents produce magnetic fields. Consequently, a current-carrying wire can attract or repel a magnet. On the other hand, magnet exerts a force on a current-carrying wire. A moving charge produces both an electric and a magnetic field.

Consider a wire (with dl as an element of length facing the direction of flow of current) with fixed line current ***I*** and the vector from the source to the point ***r*** (Figure 1.3).

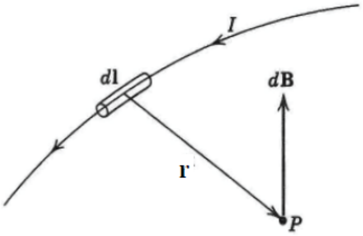

Figure 1.3: Diagram showing a wire with steady line current, I and the vector from the source to the point r (Griffiths, 1999)

Then the magnetic field, ***B*** at the point P can be expressed as

$$\vec{B} = \frac{\mu_o}{4\pi} I \int \frac{dl \times (r-r')}{|r-r'|^3} \qquad (1.8)$$

This expression is called the Biot-Savart Law. The constant μ_o is called the permeability of free space and $\mu_0 = 4\pi \times 10^{-7} N/A^2$.

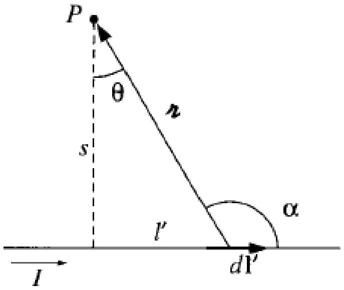

Figure 1.4: Diagram showing a long straight wire carrying a steady current, I (Griffiths, 1999)

Additionally, $l' = s\tan\theta$and therefore $dl' = \frac{s}{cos^2\theta}d\theta$. Also $s = r\cos\theta$ which resulis in $\frac{1}{r^2} = \frac{cos^2\theta}{s^2}$. Consequently, $\vec{B} = \frac{\mu_o I}{4\pi}\int_{\theta_1}^{\theta_2}\left(\frac{cos^2\theta}{s^2}\right)\left(\frac{s}{cos^2\theta}\right)\cos\theta d\theta = \frac{\mu_o I}{4\pi}\int_{\theta_1}^{\theta_2}\cos\theta d\theta = \frac{\mu_o I}{4\pi}(\sin\theta_2 - \sin\theta_1)$.

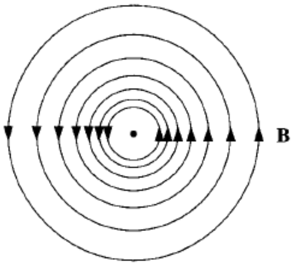

Figure 1.5: Magnetic Field due to current-carrying infinite wire (Griffiths, 1999)

For a straight infinite wire, $\theta_1 = -\pi/_2$ and $\theta_2 = \pi/_2$. Hence the magnetic field at a distance *s* from a straight infinite wire carrying a steady current *I* (Fig. 1.5) is as follows:

$$\vec{B} = \frac{\mu_o I}{2\pi s} \quad (1.9)$$

By symmetry, the magnetic field, ***B*** produced is determined only by the distance from the wire *s* and is positioned at 90 degrees to the wire. The lines of ***B*** are concentric circles around or loop enclosing the wire.

The integral of ***B*** (from equation 1.9) around a circular path of radius *s*, centered at the wire is

$$\oint \vec{B}\cdot dl = \oint \frac{\mu_o I}{2\pi s}dl = \frac{\mu_o I}{2\pi s}\oint dl = \mu_o I \quad (1.10)$$

Equation 1.10 can also be obtained for a loop with cylindrical coordinates *(s, ϕ, z)* and the current flowing along the *z* axis. For a bundle of wires, the collective line integral is

$$\oint \vec{B} \cdot dl = \mu_o I_{enc} \tag{1.11}$$

where I_{enc} stands for the total current enclosed by the integration path. This is the integral form of Ampere's Law. If the flow of charge is denoted by a volume current density, ***J*** then the enclosed current is

$$I_{enc} = \int \vec{J} \cdot d\vec{a} \tag{1.12}$$

The integral is taken over the surface bounded by the loop. Applying Stokes' theorem gives

$$\int \left(\vec{\nabla} \times \vec{B} \right) \cdot d\vec{a} = \mu_o \int \vec{J} \cdot d\vec{a} \tag{1.13}$$

Hence,

$$\vec{\nabla} \times \vec{B} = \mu_o \vec{J} \tag{1.14}$$

This expression shows Ampere's Law in the differential form. In order to find the differential equations for the magnetic field, Equation 1.14 is rewritten as follows:

$$\vec{B} = -\frac{\mu_o}{4\pi}\int \vec{\nabla}(r') \times \vec{\nabla}\frac{1}{|r-r'|}d^3\,r' \tag{1.15}$$

Given the identities $\vec{\nabla}\left(\frac{1}{r}\right) = -\frac{\vec{r}}{r^3}$ and $\vec{\nabla} \times (\varphi a) = (\nabla\varphi) \times a + \varphi(\nabla \times a)$

where φ and ***a*** are arbitrary scalar and vector functions respectively. Therefore, equation 1.15 becomes

$$\vec{\nabla} \times \frac{\vec{J}(r')}{|r-r'|} = \vec{\nabla}\frac{1}{|r-r'|} \times \vec{J}(r') + \frac{1}{|r-r'|}\vec{\nabla} \times \vec{J}(r')\vec{\nabla} \times \vec{J}(r') = 0 \tag{1.16}$$

But $\nabla \times \vec{J}(r') = 0$. Hence equation 1.16 becomes

$$\vec{B} = -\frac{\mu_o}{4\pi}\vec{\nabla} \times \int \frac{\vec{J}(r')}{|r-r'|}d^3\,r' \tag{1.17}$$

and the divergence of B is

$$\vec{\nabla} \cdot \vec{B} = 0 \tag{1.18}$$

Consider an enclosed circuit with a time-varying magnetic field. Faraday's law states that an electromotive force, ε, is induced in an enclosed circuit and is given by the negative rate of change of the magnetic flux, Φ_B through the circuit. (Equation 1.19). The time-varying magnetic field gives an electric field.

$$\varepsilon = \oint \vec{E} \cdot d\vec{l} = -\frac{d\Phi_B}{dt} \tag{1.19}$$

But $\Phi_B = \int \vec{B} \cdot d\vec{a}$. Therefore,

$$\oint \vec{E} \cdot d\vec{l} = -\int \frac{d\vec{B}}{dt}d\vec{a} \tag{1.20}$$

Equation 1.20 can be changed to a differential form by applying Stoke's theorem.

$$\vec{\nabla} \times \vec{E} = -\frac{d\vec{B}}{dt} \tag{1.21}$$

This is known as the Faraday's Law. Some books refer to it as the Maxwell-Faraday equation.

Beyond magnetostatics, the divergence of current density, J is not zero for steady currents. Hence the Ampere's law is incorrect for unteady currents. Recounting from the continuity equation and Gauss' law, Maxwell made some corrections by way of theoretical arguments.

$$\vec{\nabla} \cdot \vec{J} = -\frac{\partial \rho}{\partial t} = -\frac{\partial}{\partial t}\left(\varepsilon_0 \vec{\nabla} \cdot \vec{E}\right) = -\vec{\nabla} \cdot \left(\varepsilon_0 \frac{\partial \vec{E}}{\partial t}\right) \tag{1.22}$$

$$\vec{\nabla} \times \vec{B} = \mu_0 \vec{J} + \mu_0 \varepsilon_0 \frac{\partial \vec{E}}{\partial t} \tag{1.23}$$

For constant ***E,*** $\vec{\nabla} \cdot \vec{B} = \mu_0 \vec{J}$. Hence the correction does not change Ampere's law.

1.2.3 Maxwell's Equations

James Clerk Maxwell, who was a Scottish scientist in the 1860's and 1870's, developed the scientific theory known as the Maxwell's Equations which describe the electromagnetic wave propagation. The theory states that a time-varying magnetic field gives an electric field and a time-varying electric field gives a magnetic field. A time-varying magnetic field can be created by an accelerated charge. There are four equations which are the foundation of the Maxwell's Equations (Table 1.2).

Law	**Equation**		**Physical Interpretation**
	Differential Form	**Integral Form**	
Gauss's law for **E**	$\vec{\nabla}.\vec{E} = \frac{\rho}{\varepsilon}$	$\oint \vec{E}.d\vec{A} = \frac{q}{\varepsilon}$	Electric flux through a closed surface is proportional to the charged enclosed
Faraday's law	$\vec{\nabla}.\vec{E} = -\frac{\partial \vec{B}}{\partial t}$	$\oint \vec{E}.d\vec{S} = -\frac{d\phi_B}{dt}$	Changing magnetic flux is associated with an electric field
Gauss's law for **B**	$\vec{\nabla}.\vec{B} = 0$	$\oint \vec{B}.d\vec{A} = 0$	The total magnetic flux through a closed surface is zero
Ampere-Maxwell law	$\vec{\nabla} \times \vec{B} = \mu + \mu\varepsilon\frac{\partial \vec{E}}{\partial t}$	$\oint \vec{B}.d\vec{S} = \mu I + \mu\varepsilon\frac{d\phi_E}{dt}$	Electric current and changing electric flux is associated with a magnetic field

Table 1.2: Basic Equations for Maxwell's Equations

ρ is the free charge densities

J is the conduction current densities.

The wave equation can be obtained from the Maxwell's Equations. By applying free space constraints so that *I* and *Q* are both zero, the electric and magnetic fields are decoupled by taking second-order derivatives of equations 1.6, 1.19, 1.18 and 1.23.

$$\nabla^2 E = \mu_0 \varepsilon_0 \, {\partial^2 E}/{\partial t^2} \qquad (1.24)$$

$$\nabla^2 B = \mu_0 \varepsilon_0 \, {\partial^2 B}/{\partial t^2} \qquad (1.25)$$

Equation 1.24 and equation 1.25 have the formula of the general wave equation for a wave Ψ (x, t) traveling in the x direction with speed *v*:

$$\frac{\partial^2 \Psi}{\partial t^2} = \frac{1}{v^2}\frac{\partial^2 \Psi}{\partial t^2} \qquad (1.26)$$

Equating the speed in equation 1.26 with the coefficients on equation 1.24 and equation 1.25, the speed of electric and magnetic waves is derived, which is the speed of light symbolized with $c = \frac{1}{\sqrt{\mu_0 \varepsilon_0}} = 2.997 \times 10^8 m/s^2$.

Radio waves have the lowest frequency of the electromagnetic spectrum. In most cases, they are considered to have wavelengths ranging from 1 mm to100 km or frequencies within 3 kHz to 300 GHz. This range of frequencies includes the microwave region. Radio waves are used for satellite communication, radios, cellphones, television etc. In the case of radios, the waves also have a wide range of subcategories which include AM (Amplitude Modulation, which creates a wave of constant frequency but variable amplitude) and FM (Frequency Modulation, which creates a wave of constant amplitude but variable frequency).

Both AM and FM radio waves are used to carry radio signals in frequency ranges from 540 to 1600 kHz and from 88 to 108 MHz respectively.

Figure 1.3 shows the various nomenclature for the frequency bands in radio waves. It illustrates the relationship between frequency (f) and wavelength (λ). Every wave can be described using either its frequency or its wavelength. Frequency is inversely related to wavelength and related to the speed of light by the equation $c = f \times \lambda$, where c represents the speed of light.

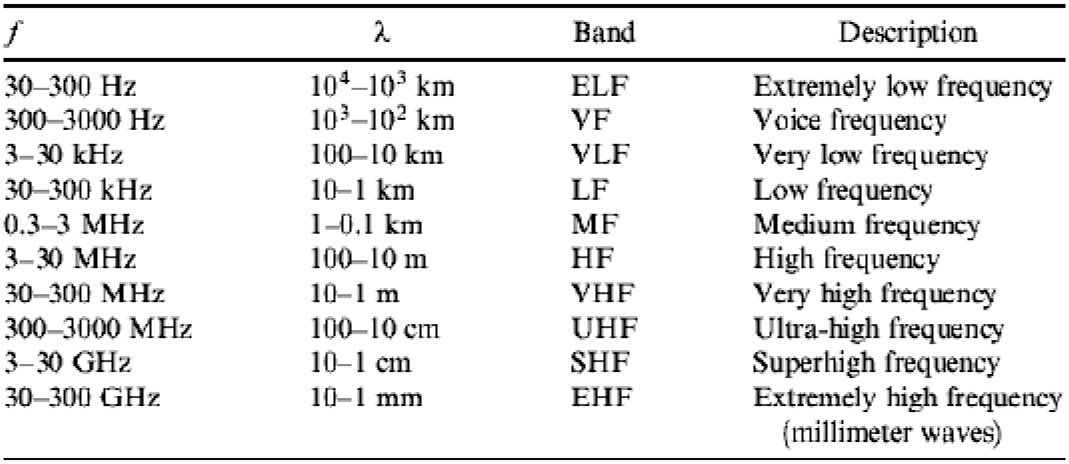

f	λ	Band	Description
30–300 Hz	10^4–10^3 km	ELF	Extremely low frequency
300–3000 Hz	10^3–10^2 km	VF	Voice frequency
3–30 kHz	100–10 km	VLF	Very low frequency
30–300 kHz	10–1 km	LF	Low frequency
0.3–3 MHz	1–0.1 km	MF	Medium frequency
3–30 MHz	100–10 m	HF	High frequency
30–300 MHz	10–1 m	VHF	Very high frequency
300–3000 MHz	100–10 cm	UHF	Ultra-high frequency
3–30 GHz	10–1 cm	SHF	Superhigh frequency
30–300 GHz	10–1 mm	EHF	Extremely high frequency (millimeter waves)

Table 1.3: Frequency Band Designations

1.3 GENERATION OF RADIO WAVES

Electromagnetic waves, in general are formed by moving electrons. The electron has an electric field shown by electric field lines. As the electron travels, for instance by means of vibrations, the moving electron also creates a magnetic field. These combined electrical and magnetic waves form the electromagnetic wave. Hence all matter produces electromagnetic waves.

Radio waves are propagated from a transmitting antenna and are intercepted by a receiving antenna. The radio wave is then converted to an electrical signal and transmitted to devices such as a radio, cellular phones, television set etc. The signal is converted to mostly sound waves which transmits the information by broadcasting through the various devices.

Radio, cellular phones, TVs etc. use radio transmission in one form or another. These radio waves can travel very fast through space because of its large frequencies and can travel through the walls because of its low wavelengths. Nevertheless, radio wave signals are weak through larger masses of earth as found in a tunnel or a cave.

1.4 PROPAGATION OF RADIO WAVES

Radio propagation refers to the behavior of radio waves when they are transferred, or are propagated from one point to another. Radio communication travels by means of electromagnetic waves traveling through the Earth’s atmosphere. Radio waves, like all other forms of electromagnetic radiation, generally travel in straight lines.

In order for radio waves to propagate, antennas are used. The antenna acts as the beginning and end of a communication circuit. An antenna is an electrical device that transforms RF signals into electric currents and are conducted across a transmitter and then the electric current is converted back into RF signals that are passed on to the receiver (Shilling, 1986).

Electromagnetic waves do not always travel directly from the transmitter to the receiver. The path of these waves rely on the frequency of the wave, the distance to be covered. There are three different forms in which radio signals can travel:

- **Line of Sight Propagation**: This is the simplest form of propagation. The signal travels in a straight line, like a beam of light. Both the transmitting and receiving antennas must be within the line of sight. This way of transmitting and receiving radio signals can be used for all frequencies above 30 MHz.

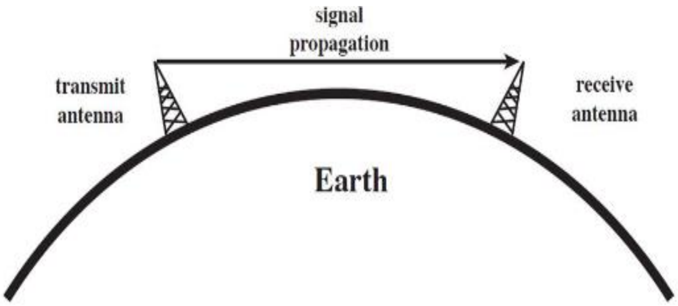

Figure 1.6: Line of Sight Propagation

The distance between the transmitter and receiver is dependent on the frequency or wavelength of the radio signal. The range can be increased by raising the height of the antenna. VHF and UHF frequencies mostly make use of line of sight communication.

- **Ground wave Propagation**: This type of propagation can speed round the Earth's curvature. This type of propagation works for most frequencies up to 2 MHz but the distance between the transmitter and the receiver will differ with geography. An example is the difference between the desert and the ocean. This way of propagation tends to be used by AM radio to propagate since it travels through short-to-moderate distances.

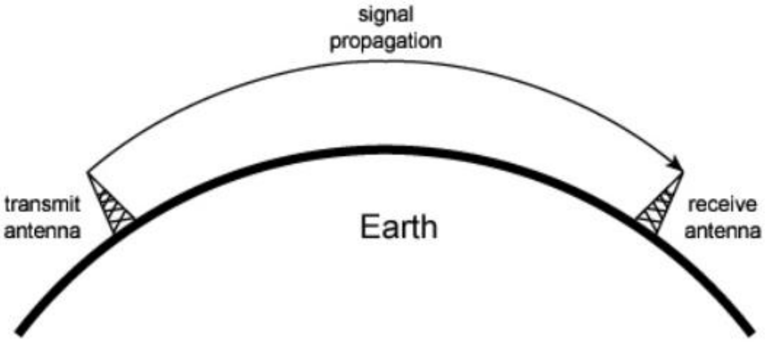

Figure 1.7: Ground Wave Propagation

- **Sky wave Propagation:** This kind of propagation has the radio signal reflected from the ionized layer of the atmosphere (ionosphere) to the earth’s surface. The signal can jump back and forth between the ionosphere and earth’s surface. This kind of propagation is used by high frequency bands (3 to 30 MHz) for short distance communication. For these frequencies, the ground slowly absorbs the signal as the frequency rises, reducing the ground wave range. Examples include international broadcasts.

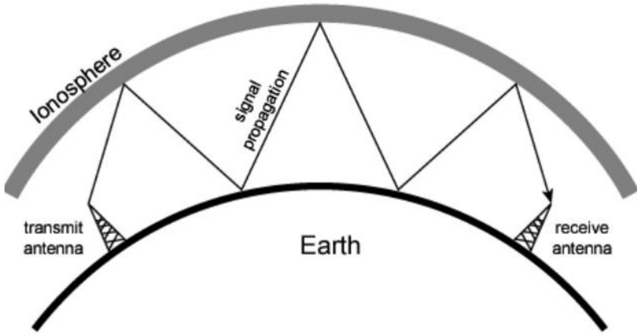

Figure 1.8: Sky Wave Propagation

1.4.1 Atmospheric Propagation

The Earth's atmosphere can be categorized into four layers. Each layer has different thermal, chemical, and physical properties (Figure 1.7). It extends beyond 560 km (348 miles) above the Earth's surface.

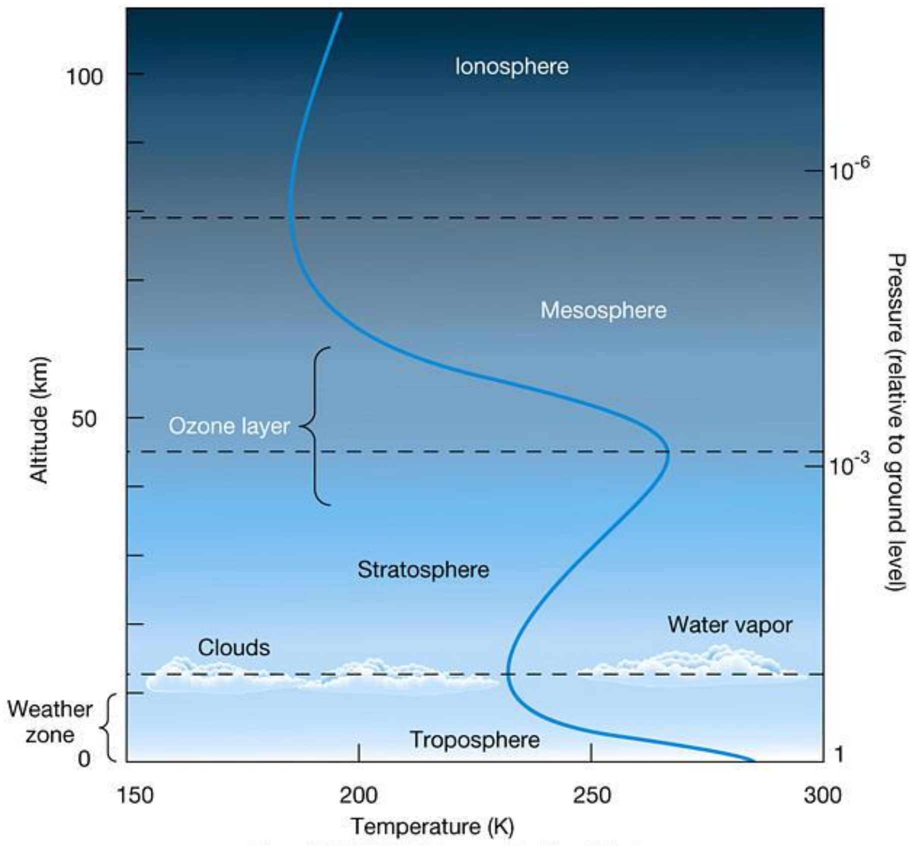

Figure 1.9: Atmospheric Layers

The troposphere is the lowest layer of the atmosphere and has an average height of 10 to 11 km. It has about 75-80% of total mass of the atmosphere. The top part of the troposphere is known as the tropopause. The temperature in this layer generally decreases with height. The earth's weather occurs in the troposphere. The stratosphere is the layer that lies above the troposphere. It has a height ranging from 11 to 45-50 km. It is composed mostly of dry stable air and makes approximately 20 to 25% of total mass. The ozone layer can be found in the stratosphere. The molecule of ozone (O_3) strongly absorbs certain ultraviolet wavelengths, and the concentration of this uv radiation from the Sun causes a rise of the temperature in the air. As a result, the temperature in the stratosphere increases with height, to about -3 ˚C (28 °F) at its upper boundary. The stratopause marks the top of the stratosphere.

The next layer is the mesosphere which lies at a height of about 45 to 92 km. The mesosphere makes up below 1% of the total mass. There is a sharp drop in temperatures to about -93 °C (-137 °F) at the top of this layer. The next layer is the ionosphere above the mesosphere. This layer has X-rays and ultraviolet rays that ionize the gases resulting in ions and free electrons. The ionosphere starts from about 60km above Earth’s surface and ranges upward to the top of the atmosphere. The ionosphere plays an important role in radio communication.

1.4.1.1 Ionospheric Propagation

The Earth’s ionosphere has the property that allows it to refract or bend radio waves passing through it. Ionospheric propagation happens within the range of frequencies from 3 to 30 MHz. The ionosphere has varying sub-regions in relation to their free electron density profile that specifies the degree of ionization. These sub-regions are known as the D, E, and F layers. The D layer is located at the lowermost region. This layer absorbs high-frequency radio waves. It generally exists during the day. As night falls, the D-layer fades then gradually disappears during the night.

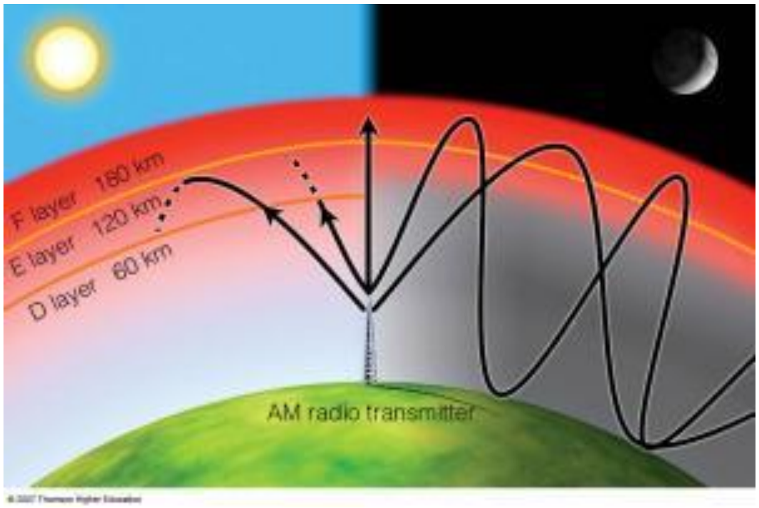

Figure 1.10: Layers of the Ionosphere over the period of a day

This allows radio waves to enter into an upper part of the ionosphere, such that the radio waves are replicated in the ionospheric region back to the earth's surface, then reflected again into the ionosphere (Figure 1.8). As a result, AM radio signals from distant stations can be received effortlessly at night. The E layer can be located above the D layer. The E layer also weakens as night falls and finally vanishes. The E layer absorbs x rays, and it has its highest at about 65 miles (105 km).

The F layer is positioned directly above the E layer, about 93 miles (150 km), and it has the highest concentration of charged particles. Though the structure of the F layer alters during the day, it is a fairly constant layer, where high levels of ultra-violet radiation are absorbed. It is made up of two parts: the lower F1 layer, and the higher and more electron-dense F2 layer.

Different types of electromagnetic radiation affect the different layers in the ionosphere. Ultraviolet rays (at wavelengths of 100 to 1000 Angstroms) ionizes the

F region, soft X-rays (at 10 to 100 Angstroms) ionize the E region, and hard X- rays (at 1 to 10 Angstroms) ionize the D region. The ionosphere is not homogeneous, and is changing continually.

1.4.1.2 Tropospheric Propagation

The troposphere is the lowest part of the atmosphere and is closest to the earth surface. The troposphere covers the space between the earth's surface to approximately 9km in height at the poles and 17km to 20km at the equator and mid-latitudes. It comprises 80% of the atmosphere's mass and 99% of it is water vapor. The earth's weather system takes place in the troposphere. The upper boundary of the troposphere is the tropopause. The tropopause divides the troposphere from the stratosphere by acting as a temperature inversion. Hence the temperature reduces with height (by approximately 6.5 ^{o}C per km) and pressure in the troposphere is highest at the surface and reduces with height. Saturation vapor pressure also declines with decreasing temperature and the water vapor content of the atmosphere declines sturdily with height.

In this environment, the troposphere tends to have an important role in the propagation of radio waves at VHF (30-300 MHz) and UHF (300- 3000 MHz) frequencies. Hence, atmospheric conditions affect the propagation of radio waves in the troposphere (Roda, 1988, Atkins, 1991).

1.5 TRANSMISSION OF RADIO WAVES

Radio waves are propagated through free space. The wave is transmitted through a straight line path. However, the path of the propagated waves is generally impeded by atmospheric conditions that cause the ray path to become curved due to the different refractive indices of the different atmospheric layers. Atmospheric gases and particles will absorb and scatter the radio wave energy. The amount of absorption and scattering will be a function of frequency and altitude above sea level (Freeman, 2007). The increasing use of microwaves for determining high data rate communication channels and determination of geophysical parameters has emphasized the need for better modeling and more accurate calculations of attenuation through clear and hydrometeor laden atmospheres.

Microwave links are useful in wireless communication by means of radio frequency (RF) transmission medium. A microwave link is a communications system that uses a beam of radio waves in the microwave frequency range to propagate information between two fixed positions on the earth. Microwave links carry cellular telephone calls between cell sites. Wireless internet service providers also use microwave links to deliver high-speed internet access to their clients. Telephone companies transmit calls between switching centers over microwave links (Elfadil, 2005). A simple one-way microwave link consists of four major elements: a transmitter, a receiver, transmission lines, and antennas. These basic components are present in every radio communications system like cellular telephones (Ghasemi, 2012).

Figure1.11: Radiowaves Transmission Media

1.5.1 Modulation

The IEEE definition of modulation is “a process whereby certain characteristics of a wave, often called the carrier signal, are varied or selected in accordance with a modulation function.” (Freeman, 1999). Another definition of modulation is the method of varying one or more parameters of a carrier signal in proportion to a baseband signal (also known as original transmission signal or message signal) carrying information to be transmitted. In most communication system practices, a message signal needs to be modulated to a higher frequency for radio transmission. Generally, no signal is made up of a single frequency sinusoid, but it extends over an array of frequencies called the signal bandwidth. For example, when an antenna is too large, modulation is applied to transmit information to a higher frequency. The baseband signal is demodulated when it reaches the point of transmission, allowing the recipient to receive the original signal.

Baseband signals are not transmitted directly. For many transmitters conveying baseband information signals simultaneously, the signals would overlap each other and there would be no simple way to distinguish between them. A possible way of solving this is by using communication at high frequencies and assigning a band of frequencies to each communication signal for its transmission. Hence the original low frequency baseband signal has to be translated into a high frequency signal before transmission. The high frequency signal (also known as the carrier signal) is then modulated. The carrier signal may be sinusoidal (continuous) or in pulses. A sinusoidal signal can be shown as

$$c(t) = A_c \sin(\omega_c t + \phi) \tag{1.27}$$

where $c(t)$ is the signal strength (voltage or current),

A_c is the amplitude,

$\omega_c = 2\pi v_c$ is the angular frequency

φ is the initial phase of the carrier signal and

t is the time.

During the modulation process, any of the three parameters (A_c, ω_c and φ) of the carrier signal can be regulated by the message signal. The three forms of modulation are:

- Amplitude Modulation (AM)

The Amplitude Modulation (AM) technique regulates the strength of the transmitted radio wave by varying the signal as it travels along the antenna. This is done to include the baseband signal information.

- Frequency Modulation (FM)

In the Frequency Modulation (FM) technique, the radio station modifies the specific frequency of the carrier signal.

- Phase Modulation (PM)

In the Phase Modulation (PM) technique the phase of the carrier signal is regulated in accordance with the information baseband signal. (Freeman, 1999).

The various techniques differ in how the carrier signal is modulated, or altered. FM signals are more advantageous than AM signals. Both AM and FM signals are susceptible to small changes in amplitude. With AM broadcasts, this results in static whiles FM broadcasts are unaffected since the audio signal is carried through changes in frequency.

1.5.2 Amplification

Amplification is the process in which the amplitude of a signal waveform is increased without changing other parameters of the waveform such as the frequency. The process is completed using an electrical circuit known as the amplifier. As a result of amplification, the signal strength is also increased. This makes up for loss in signal strength in communication systems. The signal is amplified between the source of the signal and the final endpoint depending on where the signal becomes weakened.

1.5.3 Antennae

An antenna is an electrical conductor (usually a metallic device) used to radiate and receive radio waves. It is a specialized transducer that changes RF signals to electric currents

There are two types of antennae:

- Transmitting antenna – generates RF energy from electric currents.
- Receiving antenna - collects energy from RF signals and converts it to AC signals.

In a two-way communication, the same antenna can be used for transmission and reception. All wireless systems require an antenna for radiating and receiving RF signals (Seybold, 2005). The transmitter generates the signal and the receiver detects the signal.

Transmitters and receivers are designed to operate over a limited range of frequencies. In order to transmit a signal, an antenna is used. The size of an antenna is constructed depending on the wavelength to allow the antenna to detect the time difference of the signal. For an EM wave with high frequency, the wavelength will be quite short and hence such an antenna is unfeasible to construct and operate. Hence, for signals with high frequencies and short wavelengths, the information enclosed in the original low frequency baseband signal is transformed into high frequencies before transmission.

In wireless systems, antennae are used to emit and collect electromagnetic energy. The antenna acts as the transducer between the system and free space. For many types of antennas the gain can be estimated from the physical measurements or from information of the antenna beam widths.

Reciprocity is an essential principle of antennas that states that antenna performance remains the same whether radiation or reception is considered (Seybold, 2005). This implies that the properties of the transmitting antenna or receiving antenna can be measured. The estimates of antenna gain, beamwidth, and polarization are the same for both transmit and receive based on this principle of reciprocity (Seybold, 2005).

A transmitter transfers electric charges steadily upwards and downwards along its antenna and causing the signal that is to be propagated into motion. These waves that are transmitted convey signals that are received by antennae on radios and television sets. The time-dependent changing electric field and changing magnetic field creates the magnetic field and the electric field respectively. The two travel together as a pair in the form of an electromagnetic wave into space. However, when this EM wave meets the antenna of a radio, its electric field initiates electric charges up and down on the antenna. As a result, the radio detects the travelling radio wave. The signal is then transmitted to the radio and received as sound.

1.5.4 Transmission Systems

Currently, most telecommunication systems are digital. Analog transmission is continuous whiles digital transmission is discrete. Digital transmission has signals that are propagated in pulses and represented by binary numbers, "1" or "0".

Most signals can be transmitted in either the analog or digital form. For the analog signal, the information is transported by the value or magnitude of some properties of the signal such as amplitude, frequency or a phase of a voltage, the amplitude or duration of a pulse, the angular position of a shaft, or the pressure of a fluid.

Signals heard on AM and FM radio and signals heard and viewed on television are examples of analog transmissions. In the case of the television, the video uses amplitude modulation (AM), the sound subcarrier uses frequency modulation (FM), and the color subcarrier employs phase modulation (PM) and all are in analog formats (Freeman, 1999). Digital signals can be reconstructed at their end point in the exact form they left their starting point despite any distortion along the way.

1.6 SCATTERING AND ATTENUATION OF EM WAVES

Scattering happens when the medium through which the wave is travelling contains substances with a much smaller size than the wavelength of the EM wave. These diverse phenomena result in propagation losses in the wave signal. Due to the characteristic randomness connected with such channels they are best defined with the help of statistical models (Rappaport, 2002).

Wireless communication globally is affected by microwave attenuation which has an effect on the design of the microwave link (Lee, 1995) and the calculating of the received signal level (RSL) of the RF signal from one station to another. For a given path, the kind of transmission line chosen is determined by the topography, the amount of data being transmitted, and its price. As a result, the best quality of service is not achieved in the telecommunication services in areas where microwave attenuation is a problem.

Attenuation is the measure of a loss in signal strength. Attenuation of microwaves are enhanced by atmospheric conditions such as harmattan dust and rainfall among others (wind, fog, snow etc.). They affect the consistency of satellite paths, particularly satellite paths with frequencies above 10GHz (Elfadil *et al,* 2005). Several effects of such studies have shown severe signal attenuation at frequencies in the region above 10 GHz. Attenuation is less evident at frequencies around 3 GHz (Shoewu, 2011). In Ghana, signal attenuation is highly evident in the northern part of the country due to the severe harmattan conditions in the region and in the south-western part due to the high occurrence of rainfall.

1.6.1 RAIN

Rain predominately consists of water and is also a dipole molecule. For large amounts of rainfall within the radio wave path, the strength of signal will be significantly reduced. On the other hand, rain being a dipole can be used as a reflector thus enhancing the signal.

1.6.2 FOG

Fog is caused by tiny water droplets suspended in the air. It is generally formed close to the ground due to differentiated atmospheric temperatures. Fog has properties similar to that of clouds. Fog, however causes severe weakening of the signal strength in the UHF/VHF frequency range.

The heaviest fogs tend to happen in industrial spaces where there are lots of pollution particles on which water droplets can grow. More specifically, according to the Glossary of Meteorology from the American Meteorological Society, “fog is a collection of water droplets suspended in the atmosphere in the vicinity of the earth's surface that affects visibility”. Fog decreases visibility below 1 km. **(**Howard *et al*, 1998**).** This limit is suitable for aviation purposes. Generally, for motorists a maximum of 200 m is more accurate. Transport is seriously disrupted when the visibility drops below 50 m. These three categories are known as aviation fog, thick fog and dense fog.

1.6.3 HARMATTAN

Basically, the harmattan is a dry and dusty wind which forms as a result of the pressure gradient on the west coast of the continent of Africa, i.e., the Atlantic Coast. It is typically characterized by strong winds blowing from North to South from late November to mid-March, often clocking speeds of 1.76 m/s.

The Harmattan can also be defined as a dry and dusty northeasterly trade wind which blows from the Sahara Desert over the West African subcontinent into the Gulf of Guinea between the end of November and the middle of March.

1.7 AIM AND OBJECTIVES OF STUDY

The purpose of the study is to obtain relevant parameters (visibility and rain rate) necessary for the verification of microwave attenuation models as they apply to Ghana. In order to conduct this study, the specific objectives to be performed are as follows:

- To determine the attenuation due to the effect of dust particles from visibility measurements.
- To determine the attenuation using the ITU-R rain attenuation model from measured rain rate.
- To determine any correlation between the visibility and rain rate.

- Additionally, on account of the fact that relative humidity data was measured, work is done to determine any correlation between the visibility and relative humidity.

1.8 JUSTIFICATION OF THE STUDY

Propagation of microwaves are adversely affected by atmospheric gases, rain, clouds, fog, harmattan and other atmospheric conditions. Ghana is located in the tropics which is a different environment from the temperate environments such as Europe and North America. The effects of the atmosphere on microwave signals is most severe in the tropics because of high rainfall intensities, high temperature, high relative humidity, and severe harmattan conditions which result in a more severe signal attenuation than what happens in the temperate region.

Studies have been performed in the temperate regions such as Europe and North America and it has been observed that the model being used for research in the West Africa sub-region was from literature, formulated using parameters from temperate regions. The models built from these studies are used when setting up communication links in Africa, which is in a tropical region. Also most satellite communication equipments supplied to Africa are designed based on propagation measurements made in these temperate regions, which may not meet the standards that can cope with the harsh weather conditions experienced in the tropics. This is quite inaccurate since climate conditions in the tropics are different from those in the temperate regions. For this reason, this research looks at formulating a more accurate mathematical model for microwave attenuation due to harmattan and rain for the tropics in the West Africa sub-region using measurements from parts of Ghana.

1.9 SCOPE OF STUDY

Axim in the south-western part of Ghana and Tamale in the northern part of Ghana are chosen as the study areas for measuring the impact of harmattan and rainfall on the wireless communication systems and microwave links. Axim was chosen for its high rainfall levels and Tamale was chosen because the region is well-known for its severe harmattan conditions.

Visibility and rain rate measurements were obtained using the Campbell Scientific visibility sensor and the Davis Vantage Pro weather station respectively. To calculate the attenuation due to harmattan dust and rain, the two models used for are the Zain Elabdin Model and the ITU-R Specific Attenuation Model for Rain respectively. The attenuation due to dust was obtained by setting the visibility measurements in the Zain Elabdin equation. Also, the attenuation due to rain was calculated using rain rate measurements in the ITU-R rain attenuation model. This was done for both study sites. Analysis of this data is discussed in the results. The effect of particle radius, rain rate, relative humidity and visibility on attenuation were discussed in the results.

1.10 GENERAL FORM OF THE THESIS

Chapter 1 looks at radio waves and their propagation. Also, in this chapter, the objectives of this study, justification and scope of the study were all outlined. The limitations of the study are also stated in this chapter.

Chapter 2 provides a comprehensive cover of the climate of Ghana. The Inter Convergence Zone (ITCZ) was also discussed in depth in this chapter. Literature reviews on the effects of harmattan dust, rain and fog on microwave signal attenuation are detailed in this chapter as well.

In Chapter 3, the different modelling techniques were identified and discussed. The Rayleigh and Mie approximation were discussed and demonstrated with respect to the various attenuation prediction models. The Zain Elabdin prediction model and the ITU-R rain attenuation model were also discussed thoroughly in this chapter.

Chapter 4 discusses the experimental methodology adopted for data collection and all the equipments and instruments used were discussed in detail. The study sites for this work were also discussed.

Chapter 5 dealt with the analysis of all recorded data (visibility and rainfall) and how signal attenuation for the various study sites were determined. The effects of these parameters on signal attenuation was also analyzed.

Finally, in chapter 6, discussions are detailed to interpret the effects of these weather parameters on signal attenuation. A summary of the conclusions and recommendations for future work are also detailed in this chapter.

CHAPTER 2

STUDIES OF THE EFFECTS OF DUST, FOG AND RAIN ON RADIOWAVES

In this chapter, the different climatic conditions of Ghana are discussed followed by the effects of these on radiowave attenuation. The chapter concludes with a review of some of the work done in area.

2.1 CLIMATE OF GHANA

Ghana is situated on the coast of West Africa (along the Gulf of Guinea), north of the equator. Ghana is located between latitudes of 4-12˚N and longitudes of 4 ˚W – 2 ˚E. The country has a total land area of 238,535 km^2. Ghana shares boundary with Burkina Faso to the North, Cote d'Ivoire to the West and Togo to the East (Figure 2.1).

Figure 2.1: Map of Ghana with its bordering countries

The climate of Ghana is tropical. There are two main seasons; the rainy season and dry season (harmattan). The rainy season occurs between March and September in northern Ghana.

The southern part of Ghana has two rainy seasons occurring, from March to July and from September to November. Annual rainfall ranges from about 1,100 mm in the north to about 2,100 mm in the southeast.

The dry season in Ghana happens when a dry desert wind (harmattan), blows from the northeast during the period of December to March. The harmattan lowers the humidity which leads to hot days and cool nights in the north. In southern Ghana, the effects of the harmattan are experienced in January. In most areas, the maximum temperature values occur in March and the minimum temperatures in August.

The rainfall season in the northern part of Ghana occurs from April to mid-October while the southern part of Ghana experiences its rainy season from March to mid-November. Furthermore, the southern part of Ghana has a bi-modal rainfall season: April through June and September through November. It is generally warm and relatively dry along the southeast coast; hot and humid in the southwest and hot and dry in north.

The climate of Ghana is influenced by the hot, dry and dusty-laden air mass that moves from the north east across the Sahara and by the tropical maritime air mass that moves from the south-west across the southern Atlantic ocean. The climate ranges from the bimodal rainfall equatorial type in the south to the tropical unimodal monsoon type in the north. The mean monthly temperature over most of the country always falls above 25° C. This is a result of the low latitude position of Ghana and the absence of high altitude areas. Ghana's average mean annual temperature is about 27° C. The highest temperatures, especially in the north approach 40° C. For the lowest temperatures, it drops to about 15° C. (Dickson and Benneh, 1988; Benneh *et al*. 1990).

The amount of annual rainfall for Ghana generally decrease from the south to the north. The extreme southwestern part of the country is the wettest area where the annual rainfall is over 2,000 mm. In the north, the rainfall is less than 1,100 mm per year. The south-eastern part is the driest area where the rainfall is about 750 mm. Much of the rain falls in intense storms for short periods of time, particularly at the beginning of the season resulting in heavy runoff and erosion. The annual mean relative humidity is about 80 percent in the south and 44 percent in the north (Dickson and Benneh, 1988; Benneh *et al*. 1990)

Figure 2.2: Climatic Zones in Ghana (Dickson & Benneh, 1995)

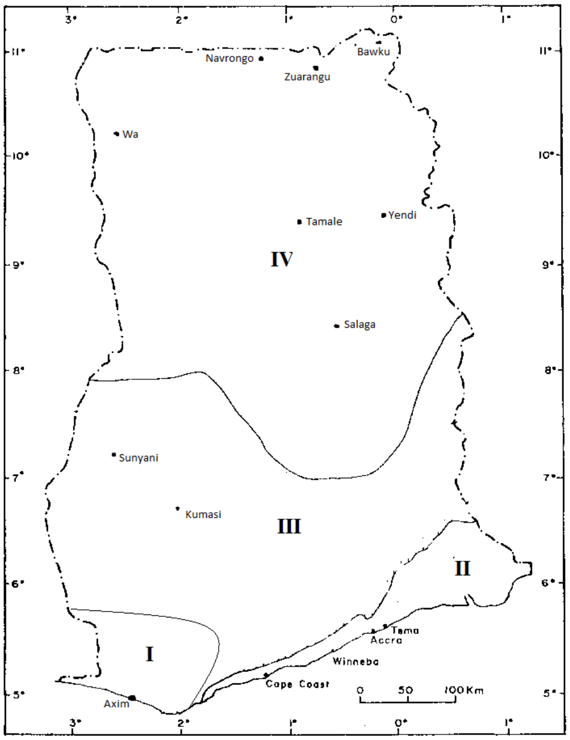

Zone I - South-western equitorial
Zone II - Dry equitorial

Zone III - West semi-equitorial
Zone IV - Tropical continental/
savanna

As shown in Figure 2.2, there are four main climatic zones marked I, II, III and IV (Dickson & Benneh, 1995). The rainfall seasons of Ghana are controlled by the movement of the inter tropical convergence zone (ITCZ).

In order to understand the ITCZ, it is important to note that the properties of an air mass are determined by two factors, namely;

- the condition of its source region (areas of high pressure)
- The air mass modifications as it travels from the source region to its destination (areas of low pressure)

The pressure difference between the source regions and the destinations produce winds and the Coriolis forces cause slight modifications (Kakane, 1998).

The climate of Ghana is influenced by two main categories of air masses; based on whether they are found on land or water. They are:

- Low level air masses/ Tropical maritime air mass/ South-Westerlies – This air mass is moisture-laden. It produces the monsoon, a humid southwest wind blowing through the Atlantic Ocean.
- High level air masses/ Tropical continental air mass / North-Easterlies. This air mass is hot and dry and gives rise to the dusty, harmattan winds which blow from the Sahara over most of West Africa from November to February.

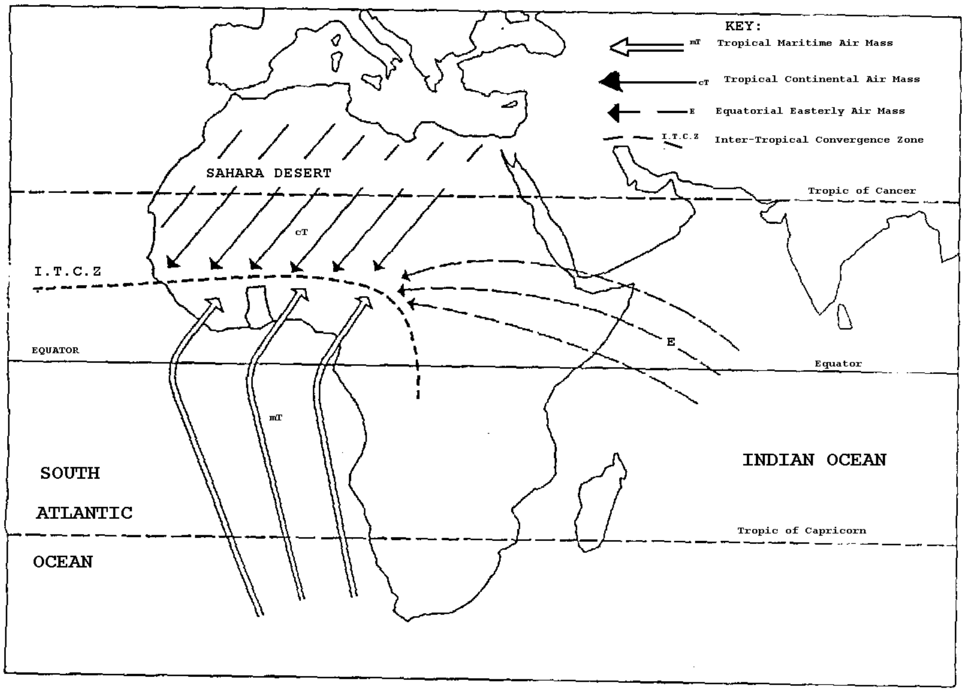

Figure 2.3: Air masses and their source regions (Dickson & Benneh, 1995)

The ITCZ is the narrow trough of low pressure discontinuity between the two pressure regions on the land and the sea as shown in Figure 2.3. The ITCZ can also be described as an area where two masses (northeast and southwest trade winds) converge and form the ascending branch of the Hadley cell. It happens globally between the equator and about 20° N/S. This results in heavy rains over the areas it passes over. The seasonal movement of the ITCZ follows the movement of the sun and moves from the north to the south. It is also responsible for the movement of the air masses. (Folland *et al.*, 1990). Hence, the rainfall seasons of Ghana are controlled by the movement of the tropical rain belt (another name for the ITCZ) as shown in Figure 2.4.

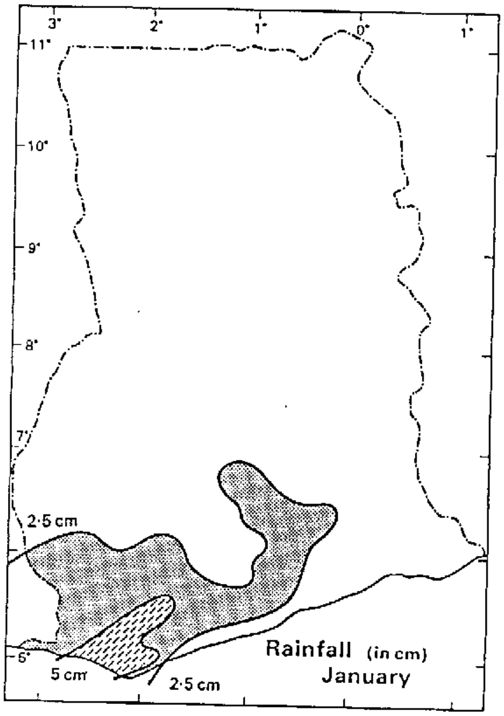

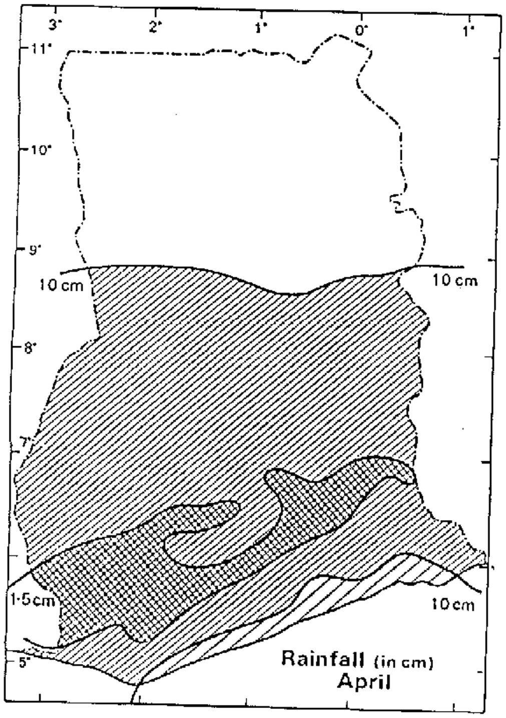

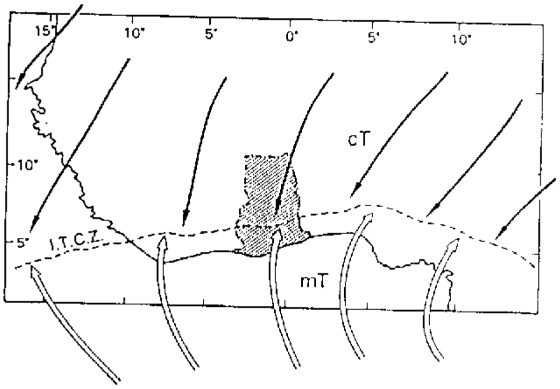

(a) Air Movements - January

— — — I.T.C.Z. Inter-Tropical Convergence Zone

→ cT Tropical Continental Air Mass

⇒ mT Tropical Maritime Air Mass

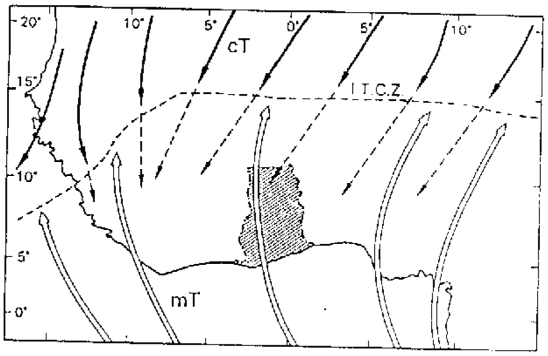

(b) Air Movements - April

(After Dickson & Benneh, 1995)

Figure 2.4: Movements of the Inter-Tropical Convergence Zone and Rainfall (Dickson & Benneh, 1995)

For regions south of the ITCZ, the dominant wind direction is south- westerly, blowing moist air from the Atlantic onto the continent. On the contrary, for regions north of the ITCZ, the dominant winds come from the north east, carrying hot and dusty air from the Sahara desert ('Harmattan'). As the ITCZ travels between its north and south positions throughout the year, the regions between these northern and southernmost positions of the ITCZ go through a shift between the two contrasting prevailing wind directions. This shift is referred to as the West African Monsoon. In northern Ghana, between May and November, the ITCZ is in its northern position and the prevailing wind is south-westerly and this causes a single wet season. Between December and March when the north-easterly harmattan wind blows, there is a dry season. The northern and central regions receive 150-250mm per month in the peak months of the wet season which lasts from July to September (Nkrumah *et al*., 2014, McSweeney *et al*., 2010).

The southern parts of Ghana have two wet seasons: the extended season from March to July, and a shorter wet season from September to November (Owusu *et al*., 2013). These seasons correspond to the northern and southern passages of the ITCZ across Ghana. The seasonal rainfall in this region differs due to variations in the intensity and movements of the ITCZ, and variations in the intensity and timing of the West African Monsoon (Nkrumah *et al*., 2014).

Zone I in Figure 2.2, also known as the South-western equatorial is the rainiest region. In this region, there are two periods of highest rainfall separated by a short dry period (known as the ‘little dry season’) usually in August. The periods of rainfall occur from April to May and from September to November with the little dry season happening from November to March. A typical example is Axim.

The second (II) zone is the Dry equatorial region. This region also has two periods of rainfall maxima. This is the driest region in Ghana. Relative humidities are higher in the rainy seasons. An example of a station is Accra.

The third (III) zone is the wet semi-equatorial region. Similar to the first zone, this zone has two rainy seasons. Temperatures and humidity are the same as in the south-western equatorial region. The annual rainfall for this region differs for this region and ranges between 1250 mm and 2000 mm. A typical example is Kumasi.

The fourth (IV) zone is the tropical continental or savannah region. This region has only one rainy season which happens from May to October. This is followed by a long period of dry season. The mean annual rainfall values range between 1000 mm and 1150 mm. The mean monthly temperatures 27 °C in August to 36 °C in March. Relative humidity values fall to as low as 20 % in the dry season and run high between 70 % and 90 % during the rainy season.

Zones I, II and III have dry periods that originate from the movement of the ITCZ as detailed above. The Dry Equatorial region extends as far as to Lome (Togo) and is referred to as the anomalous drier zone or the Togo Gap. Various explanations have been given for the existence of this gap (Dickson & Benneh, 1995, Hayward & Oguntoyinbo, 1987). The first is that the wind direction tends to be parallel to the coastline and hence the tendency for convergence and uplift is lessened. Another is that the cooler ocean surface over which the prevailing winds blow before moving onto the shore cause a lowering of the surface air temperature and reduce the tendency for uplift and rain. A third reason given is that the rain giving storms from the east deposit their rain on the Akwapim-Togo ranges. On reaching the South-eastern coastal plains they become dry winds.

Figure 2.5 shows the mean monthly rainfall distribution for the typical stations in each region. The figure shows both the little dry period in August for the Accra, Axim and Kumasi and the single rainy season for Zuarungu in the north.

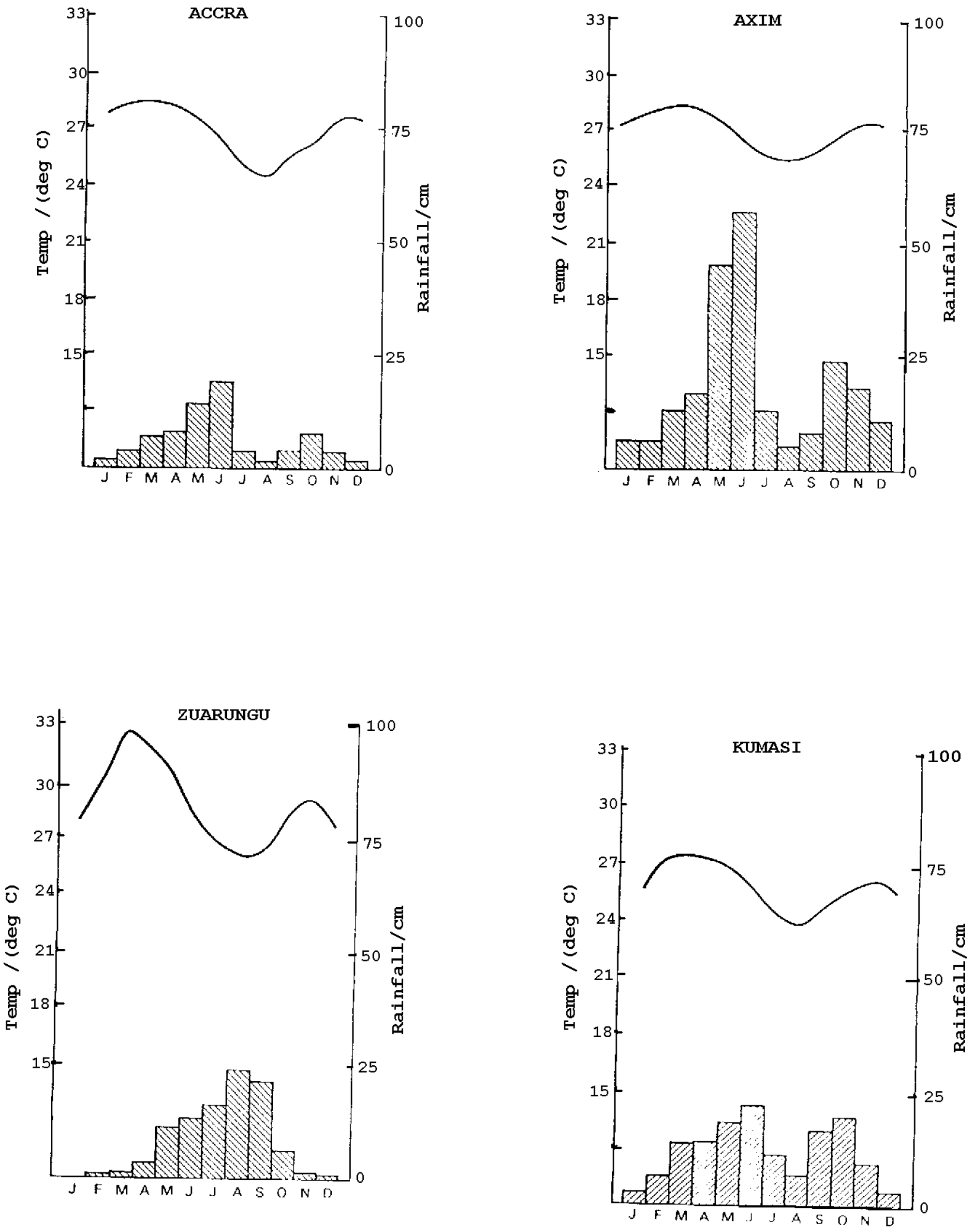

Figure 2.5: Mean Monthly Rainfall and Temperatures (Dickson & Benneh, 1995)

2.2 EFFECTS OF DUST

In 2009, Elabdin *et al*. (2009) published a paper in which a mathematical model was developed to depict the microwave signal attenuation due to dust. The mathematical model was developed to take care of all possible ratios of dust particle diameter to wavelength and calculate attenuation in the microwave band with high reliability using Mie solution of Maxwell's equations for the scattering of electromagnetic wave by dielectric spherical particles. This model aided in obtaining convenient calculations of the microwave signal path attenuation and showed the relationship between attenuation and visibility, frequency, particle size and complex permittivity. The frequency, dust particle radius and dielectric constant were directly proportional to the attenuation while the visibility was inversely proportional to the attenuation. The predicted values from the mathematical model were compared with the observed experimental values and they were in relatively optimistic agreement.

Eyo *et al.* (2003) made measurements on line-of-sight attenuation at 6.44 GHz with the intent of emphasizing microwave signal attenuation in harmattan weather conditions on a link from Akamkpa to Calabar in Nigeria. Mean signal levels were recorded and signal attenuation were calculated based on visibility, air temperature and frequency. The observed attenuations values due to harmattan weather conditions were compared with calculated fog attenuations using Altshuler model. The two results were found to be in fairly good agreement. Conclusively, microwave line-of-sight link in this region was found to be prone to signal degradation as well as fading in harmattan season.

Another study was done by Mohammed (2010) in which the effect of severe dust storms with visibility less than 1 km on some aspect of microwave propagation especially attenuation and depolarization at 12 GHz were presented. Meteorological data were collected by the Iraqi meteorological organization for 30 years in Baghdad (1958-1988) and 10 years (1978-1988) for other four stations, Nasiriyah, Basrah, Rutbah and Mousl were used in this predication. The results showed that the microwave links located at the south close to the desert affected as much as seven times more than other regions. It was found that the attenuation exceeded 1 dB for several hours while the cross polarization was in the order of -16 dB in the worst cases. The measured data was compared with available experimental measurements on line of sight and it was found that the measured values were much higher than the predicted values. This discrepancy was explained as a result of multi-path phenomena during the measurements, which are common in those areas and due to inaccuracies of the visibility measurement during the storms.

2.3 EFFECTS OF FOG

Eyo *et al.* (2003) made measurements on line-of-sight attenuation at 6.44 GHz with the intent of highlighting microwave signal attenuation in harmattan weather conditions on a link from Akamkpa to Calabar in Nigeria. Mean signal levels were recorded and signal attenuation were calculated based on visibility, air temperature and frequency. The observed attenuations values due to harmattan weather conditions were compared with calculated fog attenuations using Altshuler model. The two results were found to be in fairly good agreement. Conclusively, microwave line-of-sight link in this region was found to be prone to signal degradation as well as fading in harmattan season.

2.4 EFFECTS OF RAIN

Ojo *et al.* (2008) made predictions for rain rate and rain attenuation in order to investigate

a microwave satellite communication links at the Ku and Ka bands. In this paper, tools for the prediction of rain rate and rain attenuation were presented in the form of contour maps for Nigeria using an enormous 30-year rainfall data bank which was taken from measurements made from the coast to the arid region of Nigeria. Rain-rate maps for the country of Nigeria were developed using the models purposely designed for tropical zones while International Communications Union Radiocommunication Sector (ITU-R) models were used for the rain attenuation maps. Rain rate and rain attenuation contour maps were developed for 0.1 and 0.01% of the time using the refined Moupfouma model for rain rate maps and ITU-R 618 for the rain attenuation maps over Nigeria. The 0.1% of time of rain attenuation was needed for very small aperture terminal (VSAT) network service-availability.

In 2012, Islam *et al.* (2012) presented an improved approach of predicting rain attenuation cumulative distribution (CD) over terrestrial microwave links operating in tropical regions. The proposed method gave an improved extrapolation approach for determining the values of rain attenuation at different exceedance probability from the measured attenuation at 0.01% of the time. The experimental data consisted of measured rainfall rates and rain attenuation over six geographically spread DIGI MINI-LINKs operating at 15 GHz in Malaysia. A new set of numerical coefficients was then derived for improved rain attenuation CD predictions in the Malaysian tropical climate. As a test, a validation was implemented using rain rate and rain attenuation measurements from five Brazilian and seven Nigerian tropical locations. When tested against measurements, the proposed method seemed to suggest a significant improvement over the existing extrapolation method adopted by ITU-R Recommendations P.530-14, for the prediction of rain attenuation CD over tropical regions.

Elfadil *et al.* (2005) studied the rain attenuation prediction models for the design of microwave terrestrial line-of-sight (LOS) system. From the results, it was clearly shown that the Global Crane Prediction model predicted a much higher attenuation compared to those predicted by using ITU-R Prediction Model. This was proven from the attenuation difference of 200 dB/km at 120 GHz for the RSDs proposed by Din. In essence, all the computation from the ITU-R prediction model showed a much lower estimation compared to those from the Crane predictions.

In Pakistan’s tropical environment, Uzma *et al.* (2011) published a paper in which the line-of-sight microwave communication links were set up and operated for several years to study the microwave attenuation characteristics due to rainfall at frequencies of 15 and 38.6GHz. In this paper the cumulative distributions of microwave attenuation and the relationship between specific attenuation and rainfall rate were presented. In addition, a rain outage prediction model was proposed which not only predicted microwave radio link performance but was also useful in calculating the link degradations due to interference issues. From the results the rainfall rate, the microwave propagation characteristics, and outage predictions in Pakistan varied from the International Radio Consultative Committee predictions and ITU recommendation P530.7/8, respectively.

In 2011, Shoewu *et al.* (2011) made measurements on the line-of-sight (LOS) attenuation at 7.2GHz in Lagos for twelve months using one of the Nigerian Telecommunications radio signal. The measurement was carried out with the intent of highlighting microwave signal attenuation in harmattan and rain weather conditions. The results were presented in terms of mean signal level, received signal level and fog attenuation, rain attenuation, multipath fading, free space loss and link availability. The observed attenuation values were actually due to harmattan dust but a fog attenuation model and rain attenuation was calculated (using Altshuler's model). Also, the statistics of fade distribution show fast fading of longer duration of the order of 16 to 39 fades per hour during the harmattan period and 24 to 48 fades per hour during the period of rain. It was therefore shown experimentally that fog weather is better compare to the rain weather, due to the series fluctuation of the signal. On the other hand, transmission could be stable during rainy weather if there is space range, a larger antenna and also suitable development.

CHAPTER 3

THE RAYLEIGH AND MIE ATTENUATION MODELS FOR WAVES

In this chapter, the various scattering and absorption leading to attenuation and the various models are discussed. In addition, the effects of polarization of the wave on attenuation is also discussed.

3.1 SCATTERING AND ABSORPTION IN THE ATMOSPHERE

The atmosphere is made up of gases, which absorb electromagnetic energy at different frequencies. As electromagnetic radiation propagates though our atmosphere, it interacts with air molecules, dust particles, rain, water vapour, fog, and a number of other particles. These interactions result primarily in scattering and absorption of the EM radiation, both of which are important for studying interactions in the atmosphere. The atmospheric effects can vary significantly with location, altitude, and the path slant angle.

When a particle falls in the path of an electromagnetic wave, it can cause the radiation from the incident wave to deviate from its path. This is known as scattering. A particle in the path of an EM radiation can also be absorbed. As a result, scattering and absorption causes attenuation problems with radar and other measuring devices (Kumari, 2017).

3.1.1 Polarization of a Wave

Polarization of a wave is defined as the orientation of the lines of electric flux in an electromagnetic field. The polarization of the receiving antenna should preferably be equal to the polarization of the received wave and the polarization of a transmitted wave is equal to that of the antenna from which it originated.

3.2 THEORY OF SINGLE-PARTICLE SCATTERING

Absorption and scattering by the atmosphere affects radiowaves (microwaves), particularly those at higher frequencies. The effects of scattering becomes harsher at higher frequencies. The knowledge of these scattering characteristics is vital to the design of effective communication systems. The theory for single particle scattering is the basic theory used in mathematical modelling for attenuation.

The propagation characteristics of scattering and absorption can be modeled by assuming an incident plane wave (Elabdin et al, 2008). When an EM wave hits an object, a part of the wave is absorbed by the object and another part is scattered out.

As seen in Islam *et al.* (2010) and Ishimaru (1997), the total electromagnetic field around the scattering object is divided into an incident and a scattered field as shown in Figure 3.1

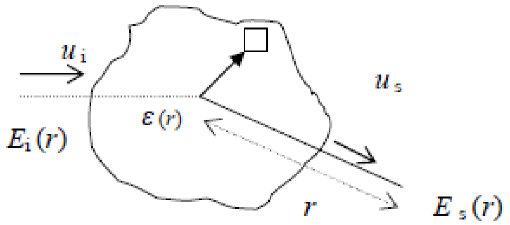

Figure 3.1: Scattering Configuration (Ishimaru, 1997)

The total amplitude of the fields at any point on the surface of a sphere is (Vishvakarma, 1993):

$$\vec{E} = \overrightarrow{E_\iota} + \overrightarrow{E_s} \tag{3.1}$$

$$\vec{H} = \overrightarrow{H_\iota} + \overrightarrow{H_s} \tag{3.2}$$

$\overrightarrow{E_\iota}$ represents the incident electric field,

$\overrightarrow{H_\iota}$ represents the incident magnet field

$\overrightarrow{E_s}$ and $\overrightarrow{H_s}$ represent corresponding scattered fields.

Where the flow of energy is involved, the poynting vector, *S*, must be used. Hence the averaged poynting vector *S* signifies the power density. The poynting vector can be separated into single terms by the separation of the total field into the incident and scattered field (Eq. 3.1 and Eq. 3.2), which then gives

$$\vec{S} = \overrightarrow{S_\iota} + \overrightarrow{S_s} + \overrightarrow{S_d} \tag{3.3}$$

where,

$$\vec{S_i} = \frac{1}{2} R \left(\overrightarrow{E_\iota} \times \overrightarrow{H_\iota^*}\right) \tag{3.4}$$

$$\overrightarrow{S_s} = \frac{1}{2} R\ (\overrightarrow{E_s} \times \overrightarrow{H_s^*}) \tag{3.5}$$

$$\overrightarrow{S_d} = \frac{1}{2} R\ (\overrightarrow{E_\iota} \times \overrightarrow{H_s^*} + \overrightarrow{E_s} \times \overrightarrow{H_\iota^*}) \tag{3.6}$$

$\overrightarrow{E_\iota}$ represents the incident electric field,

$\overrightarrow{H_\iota}$ represents the incident magnet field

$\overrightarrow{E_s}$ and $\overrightarrow{H_s}$ represent corresponding scattered fields.(Ishimaru, 1997).

The total power flow through the surface of this sphere is obtained by taking the integral of the radial component of S over the sphere. For a lossless dielectric particle that scatters, the net power flow will be zero. If it has a permittivity that is complex, the net power flow will show the absorption rate P_a of energy by the scatterer and is indicated as:

$$P_a = P_i + P_s + P_d \tag{3.7}$$

where P_a represents the integral of the radial component of S .

The medium near the particle is assumed to be lossless, consequently the total flow of the energy of the incident field is zero for every closed surface ($P_\mathrm{i} = 0$), and hence:

$$P_a + P_s = -P_d \tag{3.8}$$

Maxwell’s equations are used to sum the absorbed and scattered energy. Consequently, the extinction or total cross-section efficiency factors is defined as the ratio of the rate of removal of energy ($P_a + P_s$) to the rate of the incident energy (P_i) on a unit cross-sectional area of the scatterer. The extinction is as shown below:

$$\sigma_t = \frac{P_a + P_s}{P_i} = \sigma_a + \sigma_s = \frac{4\pi}{k} Im[u_e \cdot f(u_s, u_i)] \qquad (3.9)$$

From Equation 3.6,

k represents wave number ($k = \omega\sqrt{\mu\varepsilon} = {(2\pi)}/{\lambda}$) ,

$\left(\frac{\varepsilon}{\mu}\right)^{1/2}$ is the characteristic impedance of the medium,

$\hat{u}_e$ is the unit vector defining the polarization of the wave,

$f(u_s, u_i)$ represents the scattering amplitude function; it is a function of the direction of propagation,

u_i of the incident field and of the direction u_s from the object to the observation point (Islam et al, 2009).

3.3 APPROXIMATION METHODS/MODELS FOR SCATTERING

Scattering of electromagnetic waves by particles can be demonstrated by two theoretical frameworks:

- Rayleigh Approximation
- Mie Approximation

Rayleigh scattering generally happens when the particles producing the scattering are smaller in size than the wavelengths of the electromagnetic radiation interacting with them. Hence, Rayleigh scattering is wavelength dependent. On the other hand, Mie scattering generally occurs when the particles causing the scattering are the same size as the wavelengths of the electromagnetic radiation interacting with them.

3.3.1 Raleigh Approximation

The scattering cross section, σ_s of a small dielectric is given by Ishimaru (1999) to be

$$\sigma_s = \frac{128}{3\lambda^4}\pi^5 a^6 \left|\frac{\varepsilon-1}{\varepsilon+2}\right|^2 \tag{3.10}$$

In most instances, the scattering cross section is usually compared with the actual geometric cross section πa^2. Therefore, the Rayleigh equation is obtained as

$$\frac{\sigma_s}{\pi a^2} = \frac{8(ka)^4}{3\lambda^4}\left|\frac{\varepsilon-1}{\varepsilon+2}\right|^2 \tag{3.11}$$

(Ishimaru, 1999)

For Rayleigh approximation, it is assumed that $ka < 1$, which implies that the particle size is comparatively smaller than the radiation wavelength. For a smaller dielectric sphere as compared with wavelength, the field inside the particle is selected to be the solution of the equivalent dielectric electrostatic problem. In the Rayleigh approximation, the field inside the scattering particle is not modeled correctly (Vishvakarma, 1993; Elabdin et al, 2009). To obtain an exact solution, the scattered field reflects all the properties of the object which is no longer true for an approximation solution.

Hence, the total cross-section efficiency factors by Rayleigh approximation is expressed as:

$$\sigma_t = \sigma_s + \sigma_a = \left[\frac{8}{3}\pi a^2 (ka)^4 + 12\pi a^2 (ka) \frac{\varepsilon''}{(\varepsilon' - 1)^2 + (\varepsilon'')^2}\right] \left|\frac{\varepsilon - 1}{\varepsilon + 2}\right|^2 \tag{3.13}$$

where, a is the particle radius

k is the wavenumber ($k = 2\pi / \lambda$)

and ε', ε'' are the real and imaginary contributions respectively of the relative dielectric constant of the particles.

3.3.2 Mie Approximation

Mie scattering happens when the particles in the atmosphere are equal in size to the wavelengths being scattered. It is usually caused by particles in the atmosphere due to dust, pollen, smoke and also rain which tends to affect longer wavelengths. It is known that Mie scattering usually takes place in the lower portions of the atmosphere where there are more prevalent larger particles. These larger particles are widespread when cloud conditions are overcast.

Mie solution is a complete analytical solution of Maxwell's equations for the scattering of electromagnetic wave by dielectric spherical particles. Compared to Rayleigh scattering, Mie solutions to scattering differ by taking on all possible ratios of diameter to wavelength (Cachorro, 2001). Applications include dust particles in the atmosphere, oil droplets in water and cell nuclei in biological systems (for instance in cancer research) (Yushanov *et al*, 2013).

Mie solutions unlike Rayleigh scattering can be used to calculate attenuation in microwave wave band with high reliability mainly at higher frequencies used by new systems with greater bandwidth.

The extinction or total cross-section efficiency factors by Mie solutions can be expressed as (Collin, 1985; Elabdin et al, 2009).

$$\sigma_t = \frac{\lambda^2}{2\pi}(ka)^3(c_1 + c_2(ka)^2 + c_3(ka)^3) \tag{3.14}$$

a denotes the particle radius,

k denotes the wavenumber ($k = 2\pi / \lambda$),

λ denotes the wavelength,

and c_1, c_2 and c_3 are constants whose values depend on the real part (ε') and imaginary part (ε'') of the dielectric constant of the particles as:

$$c_1 = \frac{6\varepsilon''}{(\varepsilon'+2)^2+\varepsilon''^2} \tag{3.16}$$

$$c_2 = \varepsilon'' \left\{ \frac{6}{5} \frac{7\varepsilon'^2+7\varepsilon''^2+4\varepsilon'-20}{\left[(\varepsilon'+2)^2+\varepsilon''^2\right]^2} + \frac{1}{15} + \frac{5}{3\left[(2\varepsilon'+3)^2+4\varepsilon''^2\right]} \right\} \tag{3.17}$$

$$c_3 = \frac{4}{3} \left\{ \frac{(\varepsilon'-1)^2(\varepsilon'+2)+[(\varepsilon'-1)(\varepsilon'+2)-9]+\varepsilon''^4}{\left[(\varepsilon'+2)^2+\varepsilon''^2\right]^2} \right\} \tag{3.18}$$

3.4 SIGNAL ATTENUATION DUE TO HARMATTAN DUST

The signal attenuation due to harmattan dust is generally predicted by solving the forward scattering amplitude function of a single particle (Brussaard, 1995). The solution may be calculated by using the Rayleigh approximation or Mie solutions. The approximation method used depends mainly on the wave number and particle radius.

The attenuation of electromagnetic radiation (A_T) over a path of extent L through precipitating particles may be written as (Roger, 1976, Elabdin *et al*, 2009):

$$A_T = \int_0^L A_P \, dx \tag{3.19}$$

where A_p (dB/km) is the specific attenuation characterizing the precipitating particles.

Several authors used the following expression to determine the attenuation due to rain (Olsen *et al*, 1978, Roger, 1976, Oguchi, 1983; Elabdin *et al*, 2009):

$$A_p = 4.343 \times 103 \int_{a_{min}}^{a_{max}} \sigma_t(a) \,.\, N\,(a)da \tag{3.20}$$

where $N\,(a)\,da$ is the number of particles per unit volume of air with particles radius between a and $a + da$;

$\sigma_t\,(a)$ is the total attenuation cross section efficiency factors of particle of radius a.

3.4.1 Harmattan Dust Predicted Model

As shown from above, the attenuation of electromagnetic radiation (A_T) over a path of extent L through harmattan dust can be expressed as:

$$A_T = \int_0^L A_d dx \tag{3.21}$$

where A_d is the specific attenuation characterizing the harmattan dust which can be expressed as:

$$A_d = 4.343 \times 10^3 \int_{a_{min}}^{a_{max}} \sigma_t(a) \,.\, N\,(a)da \tag{3.22}$$

Equation 3.22 can be used to express the attenuation of electromagnetic radiation (A_d) over a path of extent L through harmattan dust.

3.4.2 Using Rayleigh Approximation

Goldhirsh (2001), in using the Rayleigh approximation method for the total cross section efficiency factor (σ_t), stated the specific attenuation due to harmattan dust, A_d as:

$$A = \frac{2.317 \cdot 10^3 \cdot \varepsilon''}{[(\varepsilon' + 2)^2 + \varepsilon''^2].\lambda} \cdot \frac{1}{V^\gamma} \tag{3.23}$$

where, V: the visibility in kilometer,

λ: the wavelength in meter,

γ: constants that depend on the type of land from which the harmattan dust originated as well as the climatic conditions,

ε' , ε'' : the real and imaginary part of the dielectric constant of the dust particles.

The Goldhirsh formulation is a modification of the Chu model which expresses the specific attenuation as a function of visibility and particle size distribution. It is suitable at wavelengths for which the Rayleigh condition is applicable which includes wavelengths corresponding to 48 GHz as a maximum frequency (Chu, 1979).

3.4.3 Using Mie solution

In order to develop a mathematical model that can calculate the signal attenuation due to harmattan dust at higher frequencies, the Mie expression for total cross-section efficiency factors (σ_t) (Equation 3.14) was selected for substitution in Equation 3.22. Therefore, the attenuation due to harmattan dust (A_d) can be written as:

$$A_d = 4.343 \times 10^3 \int_{a_{min}}^{a_{max}} \frac{\lambda^2}{2\pi}(ka)^3(c_1 + c_2(ka)^2 + c_3(ka)^3)\,.\,N\,(a)da \tag{3.24}$$

3.4.4 Dependence of Visibility

To calculate the attenuation by the Equation 3.24 involves information for the number of particles of dust N. Measuring N accurately has been found to be challenging. Alternatively, statistical data on duststorm visibility is mostly accessible. For this work, visibility values are measured. Goldhirsh (2001) states the visibility in terms of the particle density as:

$$V = \frac{5.5 \times 10^4}{N a_e^2} \rightarrow N = \frac{5.5 \times 10^4}{V a_e^2} \tag{3.25}$$

where the unit of N is particles/m^3 and a_e is the equivalent particle radius in meters.

3.4.5 Zain Elabdin Model

From the Elabdin *et al* (2009) paper, the Collin expression (Equation 3.14) was used to substitute for the total cross section efficiency factors (σ_t) and the particle density expression in Equation 3.25, A_d may also be expressed as:

$$A_d = 4.343 \times 10^3 \left[\frac{\lambda^2}{2\pi}(ka)^3(c_1 + c_2(ka)^2 + c_3(ka)^3).\frac{5.5\times10^{-4}}{Va_e^2}\right] \tag{3.26}$$

Another approximation was made, assuming that every dust particle in an actual storm may be substituted by an equivalent particle (a_e) whose radius is the mean radius for all dust particles. Using this assumption, the value of equivalent particle radius (a_e) was considered as constant and Eq. 3.26 may be expressed as follows:

$$A_d = 4.343 \times 10^3 \left[\frac{\lambda^2}{2\pi}\left(\frac{2\pi a}{\lambda}\right)^3 \left(c_1 + c_2\left(\frac{2\pi a}{\lambda}\right)^2 + c_3\left(\frac{2\pi a}{\lambda}\right)^3\right).\frac{5.5\times10^{-4}}{Va_e^2}\right] \tag{3.27}$$

Then,

$$A_d = \frac{4.343 \times 10^3 \times 5.5\times10^{-4}}{2\pi}\left[\lambda^2(ka_e)^3(c_1 + c_2(ka_e)^2 + c_3(ka_e)^3).\frac{1}{Va_e^2}\right] \tag{3.28}$$

$$A_d = 0.38\left[\lambda^2(ka_e)^3(c_1 + c_2(ka_e)^2 + c_3(ka_e)^3).\frac{1}{Va_e^2}\right] \tag{3.29}$$

$$A_d = 0.38\frac{\lambda^2}{V}[(ka_e)^3(c_1 + c_2(ka_e)^2 + c_3(ka_e)^3)\,] \tag{3.30}$$

$$A_d = 0.38\frac{\lambda^2}{V}[(c_1k^3a_e + c_2k^5a_e^3 + c_3k^6a_e^4)\,] \tag{3.31}$$

By substituting $k = 2\pi/\lambda$ in the Equation 3.31, A_d becomes

$$A_d = 0.38\frac{\lambda^2}{V}\left[(c_1\frac{8\pi^3}{\lambda}\,a_e + c_2\frac{32\pi^5}{\lambda^3}a_e^3 + c_3\frac{64\pi^6}{\lambda^4}a_e^4)\,\right] \tag{3.32}$$

This was simplified to get

$$A_d = 94.3 \times c_1\frac{a_e}{V\lambda} + 3721.2 \times c_2\frac{a_e^3}{V\lambda^3} + 23381 \times c_3\frac{a_e^4}{V\lambda^4} \tag{3.33}$$

Then

$$A_d = \frac{\alpha a_e}{V\lambda} + \frac{\beta a_e^3}{V\lambda^3} + \frac{\theta a_e^4}{V\lambda^4} \tag{3.34}$$

Where $\alpha = 94.3 \times c_1$, $\beta = 3721.2 \times c_2$ and $\theta = 23381 \times c_3$. α β and θ are constants whose values depend on real (ε') and imaginary (ε'') parts of the dielectric constant of the dust particles.

$$\alpha = \frac{565.8\varepsilon''}{(\varepsilon' + 2)^2 + \varepsilon''^2} \tag{3.35}$$

$$\beta = 3.7 \times 10^3 \cdot \varepsilon''\left\{\frac{6}{5}\frac{7\varepsilon'^2 + 7\varepsilon''^2 + 4\varepsilon' - 20}{[(\varepsilon' + 2)^2 + \varepsilon''^2]^2} + \frac{1}{15} + \frac{5}{3[(2\varepsilon' + 3)^2 + 4\varepsilon''^2]}\right\} \tag{3.36}$$

$$\theta = 3.12 \times 10^4 \left\{ \frac{(\varepsilon' - 1)^2 (\varepsilon + 2) + [2(\varepsilon' - 1)(\varepsilon' + 2) - 9] + \varepsilon''^4}{[(\varepsilon' + 2)^2 + \varepsilon''^2]^2} \right\} \tag{3.37}$$

To simplify Equation 3.34 further, the wavelength (λ) was expressed in term of frequencies (f) which is easier to use by microwave network engineers. Consequently, the specific attenuation of duststorm A_d was expressed as;

$$A_d = \frac{\alpha a_e f}{(0.3)V} + \frac{\beta a_e^3 f}{(0..3)^3 V} + \frac{\theta a_e^4}{(0..3)^4 V} \tag{3.38}$$

Finally, Elabdin et al. introduced new parameters X, Y and Z where:

$$X = \frac{\alpha}{0.3}, \quad Y = \frac{\beta}{0.3}, \quad Z = \frac{\theta}{0.3} \tag{3.39}$$

X, Y and Z were substituted into Equation 3.38 the specific attenuation due to duststorm A_d (dB/km) was expressed as:

$$A_d = \frac{a_e f}{V} (X + Y a_e{}^2 f^2 + Z a_e{}^3 f^3) \tag{3.40}$$

a_e: the equivalent particle radius in meters,

V: the visibility in kilometer,

f: the frequency in GHz and;

X, Y and Z: constants whose values depend on real (ε') and imaginary (ε'') parts of the dielectric constant of the dust particles as:

$$X = \frac{1886 \cdot \varepsilon''}{(\varepsilon' + 2)^2 + \varepsilon''^2} \tag{3.41}$$

$$Y = 137 \times 10^3 \cdot \varepsilon'' \left\{ \frac{6}{5} \frac{7\varepsilon'^2 + 7\varepsilon''^2 + 4\varepsilon' - 20}{[(\varepsilon' + 2)^2 + \varepsilon^2]^2} + \frac{1}{15} + \frac{5}{3[(2\varepsilon' + 3)^2 + 4\varepsilon^2]} \right\} \tag{3.42}$$

$$Z = 379 \times 10^4 \left\{ \frac{(\varepsilon'-1)^2(\varepsilon'+2) + [2(\varepsilon'-1)(\varepsilon'+2)-9] + \varepsilon''^4}{[(\varepsilon'+2)^2 + \varepsilon''^2]^2} \right\} \tag{3.43}$$

In completeing this model, some main assumptions made are as follows:

- Particles with radius < 1 mm have spherical shapes.
- The medium near the particles (the air) is non-conducting; hence there is no power loss in this medium.
- All particles are axially symmetrical.

By substituting applicable dielectric permittivities for the various frequencies bands (up to W band), Equation 3.40 may be altered to fit the frequency band (Elabdin *et al*, 2008).

3.4.6 THE ITU-R RAIN ATTENUATION MODEL

The Specific Attenuation Model for Rain (ITU-R P.838-3) is a model in which the specific attenuation γ_R (dB/km) is obtained from the rain rate R (mm/h) using the power-law relationship:

$$\gamma_R = kR^{\alpha} \tag{3.44}$$

γ_R represents the specific attenuation

R – rain rate

k and α – coefficients of horizontal and vertical polarization

The values of k and α can be obtained using the relations below:

$$\log_{10} k = \sum_{j=1}^{4} a_j \, exp \left[-\left(\frac{\log_{10} f - b_j}{c_j} \right)^2 \right] + m_k \log_{10} f + c_k \qquad (3.45)$$

$$\alpha = \sum_{j=1}^{5} a_j \, exp \left[-\left(\frac{\log_{10} f - b_j}{c_j} \right)^2 \right] + m_\alpha \log_{10} f + c_\alpha \qquad (3.46)$$

where f: frequency (GHz), k : either k_H or k_V, α : either α_H or α_V.

For linear and circular polarization, and for all path geometries, the coefficients k and α can be calculated from the values given using the following equations:

$$k = [k_H + k_V + (k_H - k_V) \, cos^2\theta \, cos \, 2 \, \tau] / \, 2 \qquad (3.47)$$

$$\alpha = [k_H\alpha_H + k_V\alpha_V + (k_H\alpha_H - k_V\alpha_V) cos^2\theta cos \, 2 \, \tau] \, / \, 2k \qquad (3.48)$$

where θ is the path elevation angle and τ is the polarization tilt angle relative to the horizontal (τ = 45° for circular polarization).

The ITU-R Rain Attenuation Model [ITU-R, 2001] technique is used for calculating approximately the long-term statistics of rain attenuation. The path attenuation is as shown below:

$$A_{0.01} = \gamma R d_{eff} = \gamma_R r d dB \qquad (3.49)$$

d_{eff} is the effective path length of the link,

d is the actual path length,

r is the distance factor (r is a factor which decreases in magnitude as d increases). It is obtained as expressed in equation 3.44 below:

$$r = \frac{1}{1 + {}^{d}/_{do}} \tag{3.50}$$

d_0 is a rainfall-rate-dependent factor, introduced to reflect the fact that the greater the intensity of rainfall in a storm, the smaller the physical dimensions of the storm are. It is given by (ITU-R, 2001, Hall *et al*., 1996; Pozar, 1988):

$$d_o = 35e^{-0.015}R_{0.01} \tag{3.51}$$

This is valid for $R_{0.01} \leq 100$ mm/h. For $R_{0.01} > 100$ mm/h, the value 100 mm/h is used in place of $R_{0.01}$. The prediction method defined above is considered to be effective in all parts of the world, at best for frequencies up to 40 GHz and path lengths up to 60 km.

Moupfouma (1984) proposed an empirical model for predicting rain-induced attenuation on terrestrial paths from the knowledge of 1-minute rain intensities recorded in a broad range of geographical areas and the corresponding percentages of time *p* during which these rain rates are exceeded. The rain induced attenuation on a line-of-sight path can be shown as (Moupfouma, 1984):

$$A(dB) = kR^{\alpha}d_{eff} = kR^{\alpha}rd \tag{3.52}$$

d (km) the actual path length,

d_{eff} the effective path length,

and r is a reduction factor coefficient.

CHAPTER 4

STUDY SITES, EQUIPMENT AND DATA ACQUISITION

4.1 STUDY SITES

Throughout the period between August, 2015 to January, 2018 measurements were taken for two different locations in Ghana. The choice of the study sites were based on rainfall and harmattan patterns for these areas.

Both research sites were located on the premises of a Ghana Meteorological Agency office. The Ghana Meteorological Agency (GMA), established in 1957, provides national meteorological services (Kadi, *et al*, 2011). The mission of the GMA is to provide efficient weather and climate services by collecting, processing, archiving and disseminating meteorological information to end users such as farmers, research institutions, private and public agencies etc. and advisory services to the general public on environmental issues. For this research, the Axim and Tamale research sites were chosen.

4.1.1 Axim Site

Axim is the largest town on the coast west of Takoradi. Axim is located 64 kilometers west of the port city of Sekondi-Takoradi in Western Region to the west of Cape Three Points, as shown in Figure 4.1. It is the capital of the Nzema East District, an area covering 2194 square kilometers (9.8 percent of the total area of the Western Region). It is situated almost halfway between Elubo and Takoradi. The center of the test site is at 4°51'N and 2°14'W, with elevation being about 71 meters. The Axim settlement is situated in a tranquil and sheltered natural bay with a rocky beach.

The climate of Axim is classified as tropical. There is significant rainfall for most months of the year and there is a short dry season which has little effect. The average annual temperature in Axim is 26.3 °C. About 1979 mm of precipitation falls annually.

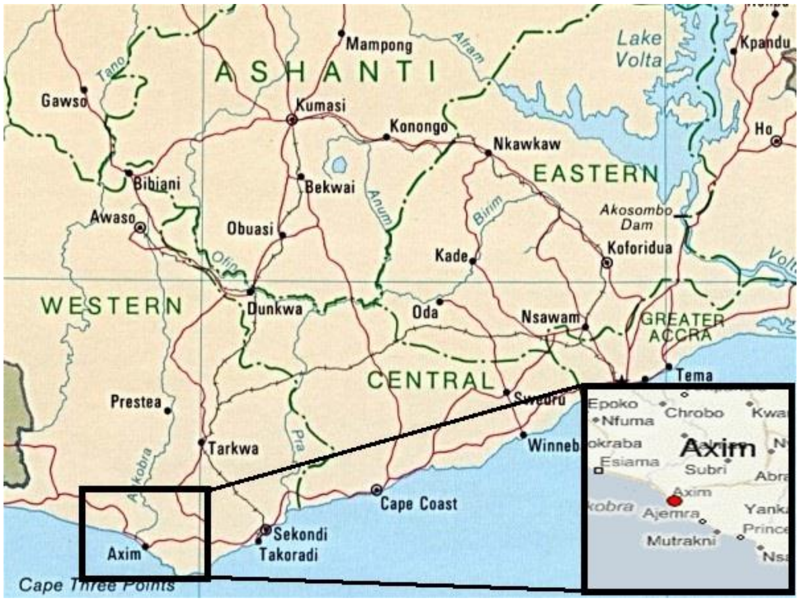

Figure 4.1: Map of Southern Ghana

Figure 4. 2 shows the location for installation of the visibility meter and the weather station at the GMA office in Axim. The GMA office is situated on a slightly elevated ground which is conducive for visibility and rainfall

measurements. The area around the office is also devoid of trees therefore there is less obstruction to the rainfall gauge and the visibility meter.

Figure 4.2: Axim research site at the GMA office

4.1.2 Tamale Site

Tamale is the capital town of the Northern Region of Ghana (Figure 4.3). Tamale is Ghana's fourth largest city. It is located at 9° 24' 2.84" N and 0° 50' 21.48" E and it is situated at an elevation of 196 meters above sea level. It is estimated to have a 2013 projected population of 360,579 according to the 2010 census. The town is located 600 km (370 miles) north of Accra.

According to the Köppen's climate classification, the climate of Tamale consists of a tropical wet and dry climate. There exists one rainy season from April to September or October, with the highest rainfall happening in July and August.

The dry season is generally from November to early April. The season is influenced by the dry north-easterly (harmattan) winds, while the rainy season is influenced by the moist south-westerly winds. The mean daytime temperatures range from 28 (December and mid-April) to 43 (March, early April) degrees Celsius, while mean nighttime temperatures range from 18 (December) to 25 (February, March) degrees Celsius. The mean annual daily sunshine is about 7.5 hours. This lowers the humidity causing hotter days and cooler nights (UNDP, 2013).

Figure 4.3: Map of Northern Part of Ghana

The office of the GMA in Tamale is located at the Tamale airport. All installations and measurements were taken on the premises of the GMA office (as shown in Figure 4.4). The instruments were installed in an enclosed space beside other meteorological equipment owned by the GMA.

Figure 4.4: Tamale research site at the GMA office

4.2 EQUIPMENT USED

In order to study the attenuation of microwave links at 3GHz-10GHz in Axim and Tamale visibility and rain rate were measured. The equipments used for these measurements include a

- Davis Vantage Pro 2 Weather Station
- MiniOFS Visibility Sensor
- Campbell Scientific CS120 Visibility Sensor
- Campbell Scientific CR1000 Datalogger

Visibility and rain rate measurements were recorded between the periods from August, 2015 to January, 2018.

In Axim, the MiniOFS visibility meter and one of the Davis weather stations were installed to measure/ record visibility and rain rate respectively. As stated earlier, the installations were set up at the Ghana Meteorological Agency office located in Axim.

A Campbell Scientific Visibility Meter and a Davis Weather Station were set up and put in operation at the GMA office located at the Tamale Airport. Visibility was measured alongside the rainfall rate with one minute intervals in this location between the periods from April, 2016 through January, 2018. The weather station is equipped for measuring temperature, relative humidity, dew point, wind speed, direction and chill, air density and parametric pressure etc.

4.2.1 Campbell Scientific CS120 Visibility Sensor

The visibility sensor used for this research was the Campbell Scientific CS120 (Figure 4.5). The CS120 is an infrared forward scatter visibility sensor used for automatic weather stations including road, marine and airport based stations. It uses the well-established forward scatter system for visibility measurement, employing a 42^{o} scatter angle. The CS120 makes use of high speed sampling to decrease the number of missed events such as rain and hail and improves response to other suddenly changing conditions.

Figure 4.5: Campbell Scientific CS120 Visibility Sensor

The CS120 incorporates the principle of forward scattering, which is the determining of the extinction coefficient (visual range) by measuring the amount of light scattered in the forward direction by atmospheric particulates (Muench, 1974).

The forward scatter sensor measures the amount of light scattered at an angle of 42 degrees (in the case of the CS120) by small particles suspended in its sample volume, or large particles passing through its sample volume. The amount of scattering is correlated to the quantity of particles in the volume of air being sampled. The sample volume is defined by the intersection of the transmitted beam of light and the receiver's field of view (Clark *et al*, 2012).

For forward scatter visibility sensors, absorption cannot be measured directly. However, the relationship between the amount of absorption and the amount of forward scatter under various weather conditions has been obtained by experimentation. By adding a back scatter receiver and thermometer to a forward scatter instrument, current weather can be identified, and additional factors for absorption added into the extinction coefficient calculations.

Visibility is influenced by the particulates existing in the atmosphere, such as fog droplets, dust particles or raindrops. It is also determined by lighting conditions and characteristics of the object such as contrast (daytime) or brightness (if a light).

4.2.2 Mini OFS Optical Sensor

The Mini OFS optical fog sensor is a low price optical sensor. It is one of the cheapest visibility sensors on the market. It has a lower performance than other visibility meters. The Mini OFS can be used to measure visibility. The sensor is for particles in the atmosphere at a distance of about 25cm in the line of sight of the sensor. These microscopic particles include raindrops, fog, snow and harmattan dust.

In order to keep the electronics dry, there exists a membrane ventilator that retains the pressure inside the sensor at the same level as the outside pressure. The membrane ventilator prevents water from leaking into the sensor. The mini OFS can measure visibilities from 20 m to 4 km.

Figure 4.6: MiniOFS Optical Sensor

The sensor is mounted horizontally and facing north on a pole. The line of sight of the sensor closer than 5 - 10 m should be clear. The sensor comes with a PMMA plastic mounting bracket which isolates the sensor electrically reducing the risk for surge currents. It has a connected 6 m 5-wire cable.

4.2.3 Davis Vantage Pro 2 Weather Station

The Davis Vantage Pro 2 weather stations include a console and a versatile Integrated Sensor Suite (ISS).

The ISS gathers outside weather data and sends the data to a Vantage Pro 2 console. The wireless ISS is powered by solar panels and sends data by radio. The cabled ISS sends data by cable to one cabled Vantage Pro 2 console and receives power through the console. For this work, the wireless ISS is used.

The Vantage Pro 2 ISS (Figure 4.7) includes a rain collector, temperature sensor, humidity sensor and anemometer. The temperature and humidity sensors are mounted in a passive or fanaspirated radiation shield to reduce the effect of solar radiation on the sensor readings. The anemometer measures wind speed and direction and can be mounted separately from the rain collector and installed adjacent to the ISS or installed separately. The anemometer has been wind-tunnel tested to 200 mph.

The transmitter shelter encloses the "brain" of the ISS: the sensor interface and the transmitter. It collects outside weather data from the ISS sensors and then transmits the data to the wireless console.

Figure 4.7: Vantage Pro 2 Integrated Sensor Suite (ISS)

The console (Figure 4.8) is designed to give extremely accurate readings. Installing the console is relatively simple but care has to be taken in setting it up. Together with the ISS, assembling the Vantage Pro 2 correctly from the start will help ensure that all its features operate correctly with minimal time and effort.

Figure 4.8: Vantage Pro 2 Console

The use of the AC adapter in the wireless Vantage Pro 2 consoles are optional. Each console carries three C-cell batteries which power a wireless console for an estimated period of up to nine months. The Vantage Pro 2 weather station is designed to withstand extreme weather.

4.2.4 Campbell Scientific CR1000 Datalogger

The CR1000 datalogger (shown in Figure 4.9) is made up of a measurement and control module and a wiring panel. It operates with an external display and power supply. The CR1000 datalogger has a low power consumption which allows it to operate for long periods of time on a battery recharged with a solar panel.

The datalogger’s module measures sensors, initiates direct communications and telecommunications, reduces data, controls external devices, and stores data and programs in on-board, non-volatile storage. Its electronics are shielded from radio frequencies. It has a battery-backed clock to ensure precise timekeeping. The module can run measurement and communication functions concurrently. The on-board, BASIC-like programming language supports data processing and analysis routines. Most CR1000 data loggers have a 4 MB memory.

The CR1000 has several channel types and hence is compatible with almost every available sensor, including thermocouples, SDI-12 sensors, and 4 to 20 mA sensors (using a terminal input module). Adding a custom ASIC chip expands its pulse count, control port, and serial communications capabilities. The CR1000's input and output ports can be paired for transmission and receiving, allowing serial communications with serial sensors and devices.

The CR1000 communicates with a computer through direct connect, ethernet interfaces, multidrop modems, short-haul modems, phone modems (land line, digital cellular, and voice-synthesized), RF telemetry, and satellite transmitters (Argos, Iridium, and Inmarsat). Data can be viewed on a computer using a compatible software: PConnect or Loggernet. Its communication ports include a CS input/output, RS-232 and a parallel peripheral.

Figure 4.9: CR1000 Measurement and Control Datalogger

4.3 Methodology

Prior to the installation of the various instruments at the study sites, test runs for each of the weather station were done at the Physics Department of the University of Ghana. This was done to ensure all proper installation measures were applied to certify the proper operation of the instruments.

The sensor interface of the ISS can be found in the transmitter shelter on the front of the ISS station. . All connections for the weather sensors are enclosed in the ISS. The sensor interface was checked to ensure that all sensors were connected correctly.

Figure 4.10: Setting the Transmitter ID for communication between the ISS and the console

The Vantage Pro2 console can collect data from up to 8 different wireless stations. The default Transmitter ID for the ISS and console is 1. Generally, it will not be compulsory to change the Transmitter ID. The console and ISS should typically begin communicating automatically when powered up. In the case where the console and ISS are not communicating, the Transmitter ID has to be manually set. For this test run, the console and ISS communicated effectively. As a further check, different IDs were selected to check for communication using different IDs to set up the console.

A protective cage (Figure 4.11) was made in the department of Physics, University of Ghana to guard the weather station.

Figure 4.11: Positioning the protective cage around the weather station at the Physics Department, University of Ghana

Figure 4.12 shows the complete test installation of the ISS of the weather station. The ISS was effectively communicating with the console which was set to a transmission ID of 1.

Figure 4.12: Complete ISS setup communicating with console

With the successful test installations, the weather stations were installed at the different study sites; Axim and Tamale.

Rainfall rate measurements were recorded using the Davis Vantage Pro 2 Weather Station that was installed at the two study sites. This is needed for the study sites in order to predict accurate rain attenuation for the two different study sites.

One of the Davis weather station Vantage Pro 2 was setup at the offices of the Ghana Meteorological Agency in Axim and the other was installed at the Ghana Meteorological Agency office located at the airport premises in Tamale.

Figure 4.13: Setting up the Davis Vantage Pro 2 Weather Station at the Axim site

Figure 4.14: Installed Vantage Pro 2 weather station at the Tamale site

The CS120 sensor was securely mounted on a pole. The pole was extended to a height of 1.5 m approximately and clamped between the DSP plate and brackets by tightening using the nuts provided.

Before installing the Campbell Scientific visibility sensor, the ground consistency was checked to ensure it was not loose and could support the concrete foundation and mount. The concrete foundation was created for the mount to be installed on it (as shown in Figure 4.15).

Figure 4.15: Concrete foundation for mount installation

Its dimensions were at least 600 mm square and 600 mm deep. Four 12 mm diameter holes were drilled to a depth of 77 mm using the mount base as a template and the debris in the holes were cleaned. Washers and nuts positioned on the ends of the wedge anchor supplied (to protect the threads during installation).

Figure 4.16: Fully mounted visibility sensor

The installation of the CS120 visibility sensor was fully completed with its installation on the concrete foundation. All necessary connections were done to ensure that the correct visibility measurements were recorded. The CR1000 datalogger was used to interface between the CS120 and the computer to record the visibility measurements using the Loggernet program.

The CS120 is a robust instrument that operates uninterrupted weather monitoring for years. The sensor has been calibrated at the factory and for this research, no calibration was redone on site. The lenses were cleaned at least every six months because of the dust contaminants in the research sites. This was to guarantee that the lenses were free from contaminants and keep the sensor working efficiently. The sensor can self-diagnose dirty lenses and give a prompt in its output when the lenses are contaminated to such a degree that its visibility measurements may be affected.

Figure 4.16: Set up the CS120 Visibility Sensor and Vantage Pro 2 Weather Station at the Tamale site

Figure 4.16 shows the full setup of both the visibility sensor and the weather station at the Tamale site. The visibility is measured using the Campbell Scientific visibility sensor and the Vantage Pro 2 weather station measured barometric pressure, temperature, humidity, rainfall, rain rate, wind speed and direction, UV/solar etc. Highs and lows and/or totals or averages of all parameters were recorded.

4.4 DATA ANALYSIS

The measured rainfall and visibility data were collected, reviewed and evaluated after every few months. The data analysis process started with the collection of all relevant and useful data, organization of all relevant data gathered from the different study sites.

The rain data and the visibility data at one-minute and one-minute intervals respectively were collected at both the Axim site and the Tamale site located at the Tamale airport from August, 2015 to January, 2018. The attenuation due to dust was obtained by setting the visibility measurements in the Zain Elabdin equation whiles the attenuation due to rain was calculated using rain rate measurements in the Specific Attenuation Model for Rain (ITU-R P.838-3) .

The effect of particle radius, rain rate, relative humidity and visibility on attenuation were discussed in the results. A final step conducted was interpretation of the data which involved determining the meaning of the information gathered.

CHAPTER 5

RESULTS AND DISCUSSIONS

In this chapter, all the experimental results from the experiments outlined in chapter 4 are presented. As mentioned in Chapter 1, in performing this research, the objectives stated were as follows:

- To determine the attenuation due to the effect of dust particles from visibility measurements.
- To determine the attenuation using the ITU-R rain attenuation model from measured rain rate.
- To determine any correlation between the visibility and rain rate.
- Additionally, on account of the fact that relative humidity data was measured, work is done to determine any correlation between the visibility and relative humidity.

The data collected during this research work was made up of visibility measurements, rainfall measurements, as well as other meteorological data. Rainfall data was set to be recorded every 5 minutes. Additionally, other meteorological data such as humidity, wave speed and direction, solar irradiance and others were recorded along with the rainfall measurements.

In the course of research, data collection for some periods were not obtained as a result of power fluctuations and equipment malfunctioning. However, there was enough data recorded to complete the research. Due to the large amounts of data recorded, it became necessary that visibility and rainfall values were averaged before analysis work was done.

Hence, an analysis of the visibilities and rain rates in Axim and then Tamale are presented. The analysis presented includes the effect of mainly visibility and rain rate on microwave attenuation. Also the effects of particle size and relative humidity were discussed in the results. The implications of these effects, in line with the objectives of this work, are also discussed in this chapter.

5.1 Signal Attenuation Analysis

Long term visibility data were recorded in Axim and Tamale. Axim is situated in the Western Region whiles Tamale is in the northern region of Ghana. Harmattan is more frequent in Tamale whiles rainfall is highest in Axim. The main aim of visibility data collection was to use the available data to estimate the effect of harmattan dust on microwave attenuation in parts of Ghana.

It is recalled in Chapter 3, the specific attenuation due to harmattan dust proposed by Zain is expressed as:

$$A_d = \frac{a_e f}{V} (X + Y{a_e}^2 f^2 + Z{a_e}^3 f^3) \, [dB/km]$$

5.2 Axim Measurements

Visibility data as a result of the harmattan dust and rainfall rate data were measured and recorded. The data was analyzed using the respective attenuation models chosen for calculating the attenuation.

5.2.1 Harmattan Dust Results

Visibility data was recorded over a period between 2015 and 2016 in both Axim and Tamale. The recorded data was used to calculate the signal attenuation using the Zain Elabdin model at the different frequency bands.

5.2.1.1 Attenuation for the Different Frequency Bands

A more simplified attenuation formula was obtained by separating the general attenuation formula into separate formulae to calculate the attenuation due to harmattan dust for each frequency band. This makes the formula more useful for microwave network designers and engineers. The general formula for the signal attenuation due to harmattan dust particles depends on visibility, frequency, dust particles radius and dielectric constant as seen in Equation 3.38. The dielectric constant values of the dust particles are important in the determination of attenuation for the different frequency bands.

Various researchers have measured the refractive index of sand and dust samples (Chu, 1979, Ghobrial, 1980, Ruike *et al*, 2003) which were used for further approximations in the new subdivided formulas. It was assumed that a single value of the refractive index can be fitted for all frequency ranges in specific microwave band (Islam *et al*, 2010).

Frequency Band	**Frequency Range (GHz)**	**ε', ε''**
S-band	2 – 4 GHz	4.56, 0.251 (Ghobrial, 1980).
C-band	4-8 GHz	4.56, 0.251 (Chu, 1979)
X-band	8 – 12 GHz	5.73, .415 (Ruike, 2003)
Ku-band	12 – 18 GHz	5.5, 1.3 (Ruike, 2003)
K-band	18 – 26.5 GHz	5.1, 1.4 (Ruike, 2003).
Ka-band	26.5 – 40 GHz	4, 1.325 (Ruike, 2003)
W-band	56 – 100 GHz	3.5, ε'' = 1.64 (Ruike, 2003)

Table 5.1: Dielectric constants for the different microwave frequency bands (Islam *et al*, 2010)

For visibility data recorded in Axim for the month of December, 2015, the attenuation due to harmattan dust for the different frequency bands was calculated.

The dielectric constants used for all calculations are as shown in Table 5.1. The frequency bands range from 10-100 GHz. The specific attenuation as a result of dust was calculated for the averaged visibility values of one set of collected data recorded in Axim.

Figure 5.1 to Figure 5.9 illustrate the graph of the signal attenuation against frequencies in the different frequency ranges.

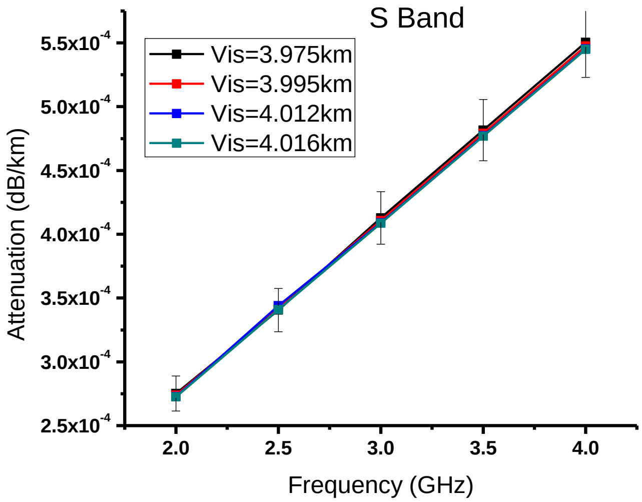

Figure 5.1: Signal Attenuation versus Frequency at S-Band for Different Visibilities in Axim

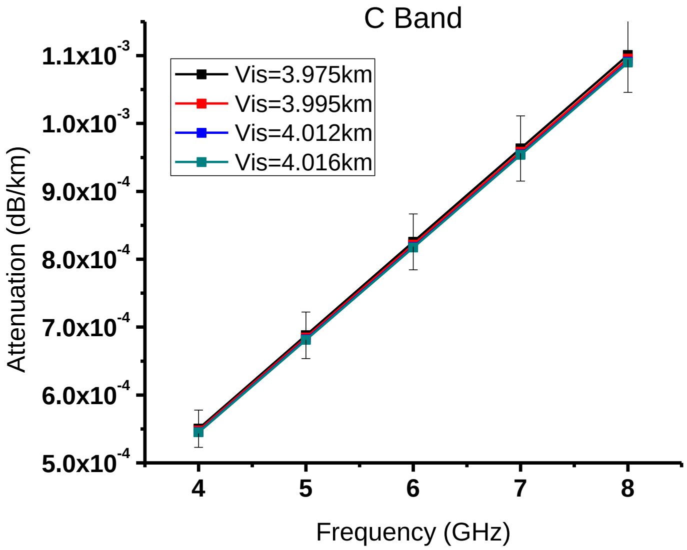

Figure 5.2: Signal Attenuation versus Frequency at C-Band for Different Visibilities in Axim

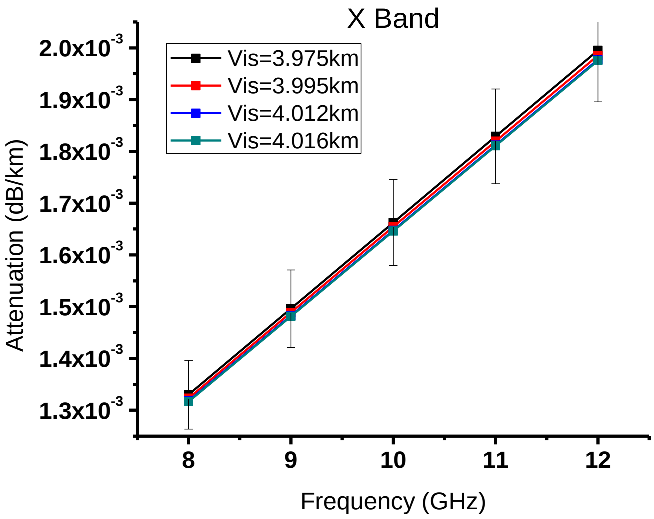

Figure 5.3: Signal Attenuation versus Frequency at X-Band for Different Visibilities in Axim

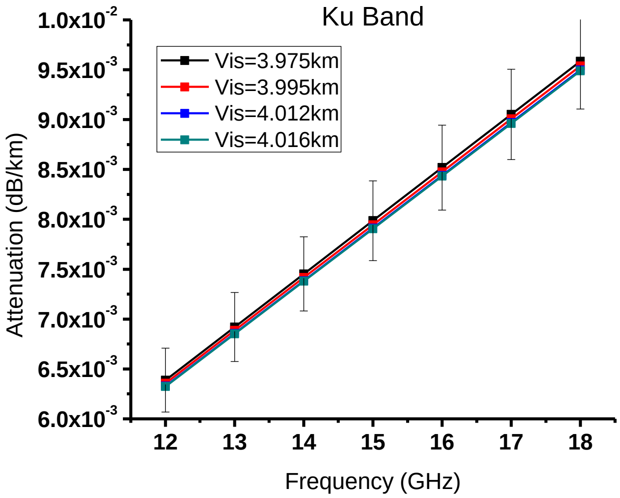

Figure 5.4: Signal Attenuation versus Frequency at Ku-Band for Different Visibilities in Axim

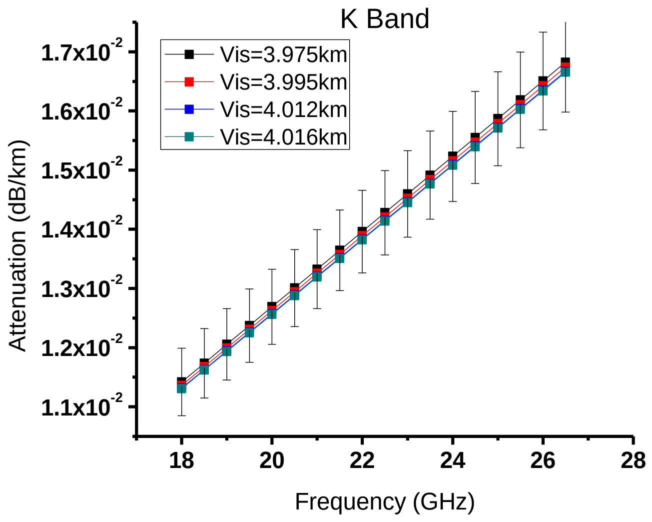

Figure 5.5: Signal Attenuation versus Frequency at K-Band for Different Visibilities in Axim

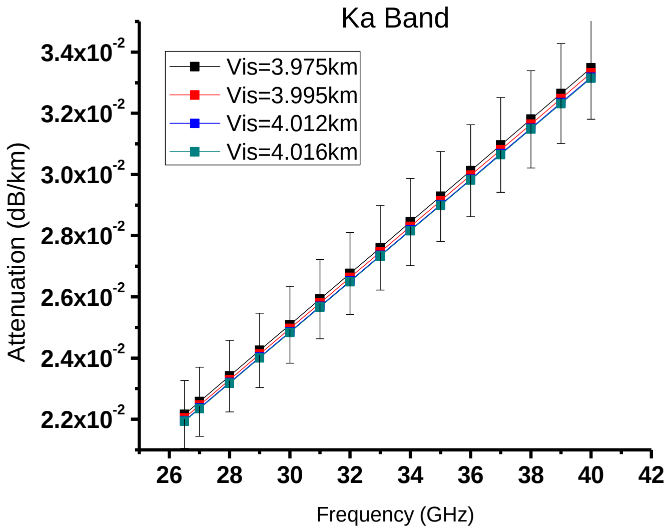

Figure 5.6: Signal Attenuation versus Frequency at Ka-Band for Different Visibilities in Axim

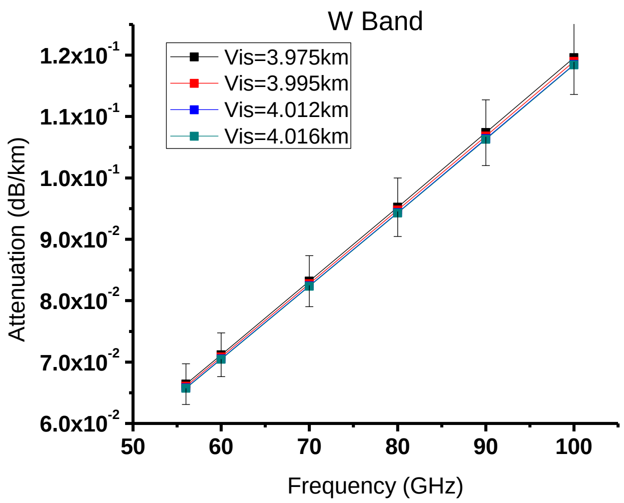

Figure 5.7: Signal Attenuation vrs Frequency at K-Band for Different Visibilities in Axim

From Figures 5.1 to Figure 5.7, it was observed that the signal attenuation increased with increasing frequency bands. The same trend run through for the different frequency bands as shown. The attenuation values increase with the different increasing frequency band ranges.

In the Elsheikh *et al* (2010) paper, the Zain Elabdin dust/sand storm prediction models were examined based on different probability density functions obtained from different papers (Ghobrial 1980, Haddad et al, 1983, Row et al, 1985, Patterson et al, 1977, Grams et al, 1974, Bilford et al, 1971) in order to reflect the various ranges of dust particle sizes that may exist during the dust storm (Elsheikh *et al*, 2010).

Figures 5.8 to 5.11 show the attenuation against frequency for varying dust particle sizes. Attenuation values were obtained for each average visibility measured. The particle size of 0.7 um was obtained from a Hughes (2015) paper and the 10um was the particle size used for this work. The other particle sizes were varied to observe their effect on attenuation.

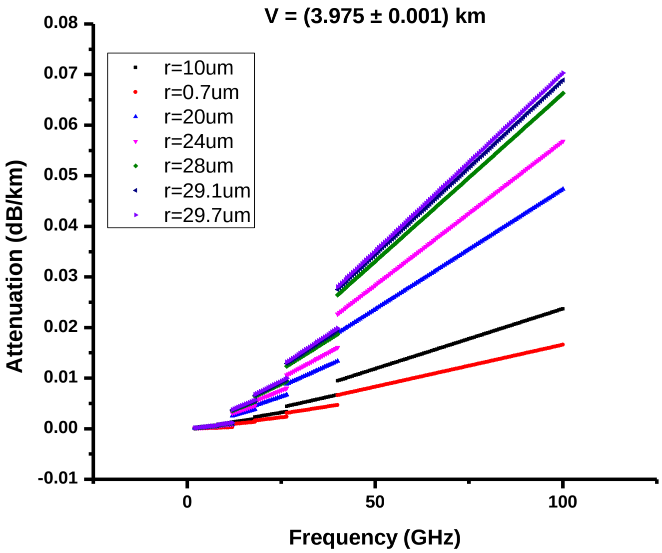

Figure 5.8: Signal Attenuation due to harmattan against Frequency at Vis = 3975.648936m for different radius sizes

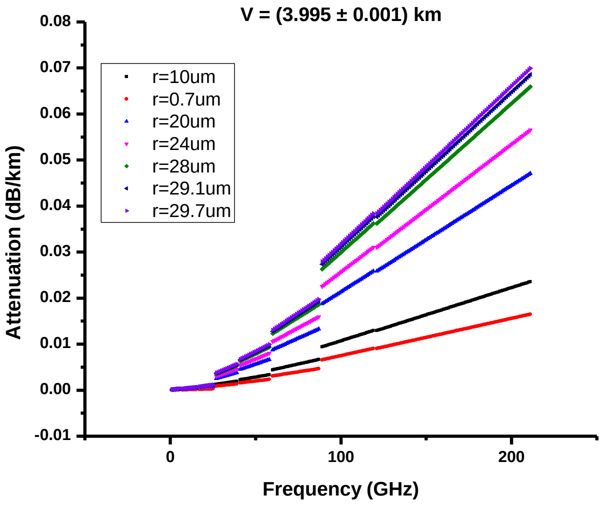

Figure 5.9: Signal Attenuation due to harmattan against Frequency for Vis = 3995.711m at different radius sizes

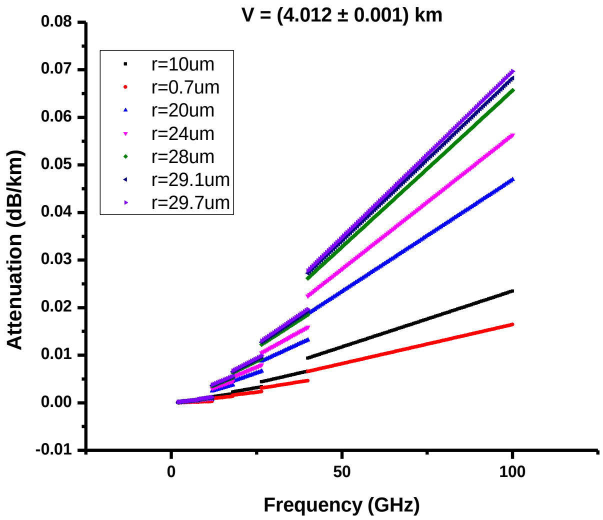

Figure 5.10: Signal Attenuation due to harmattan against Frequency for Vis = 4012.395m at different radius sizes

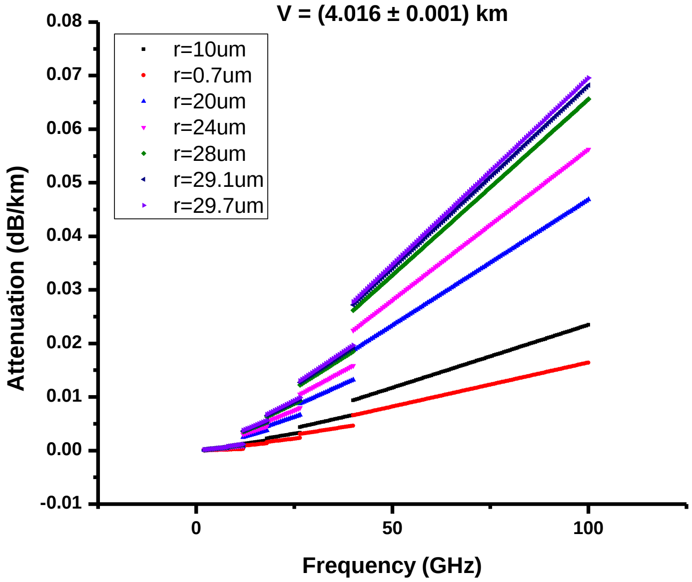

Figure 5.11: Signal Attenuation due to harmattan against Frequency for Vis = 4016.027m at different radius sizes

It was found that the signal attenuation remained within the same range of 0 dB/km to 0.8 dB/km for all the four varying average visibilities across all the different particle. Generally, it is observed that attenuation increased with increasing frequency. Some discontinuities were observed in the trend. This was as a result of the transition between different frequency bands.

The graph obtained is as expected from the equation, which is frequency is directly proportional to attenuation.

5.2.2 Rain Rate Measurements

Measurements of the rain rate in Axim during the research period was recorded and used to calculate the microwave attenuation within the area. The rain rate was recorded with a 5-minute interval. In analyzing the data, the average monthly values were calculated and the graphs are as shown below in Figure 5.12.

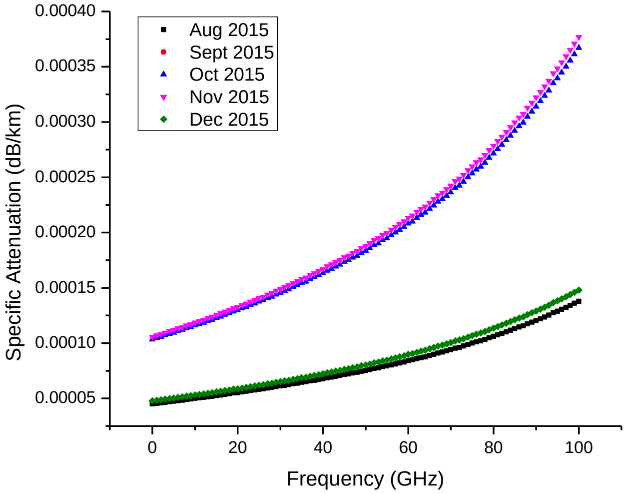

Figure 5.12: Graph of Rain Attenuation versus Frequency from August - October 2015

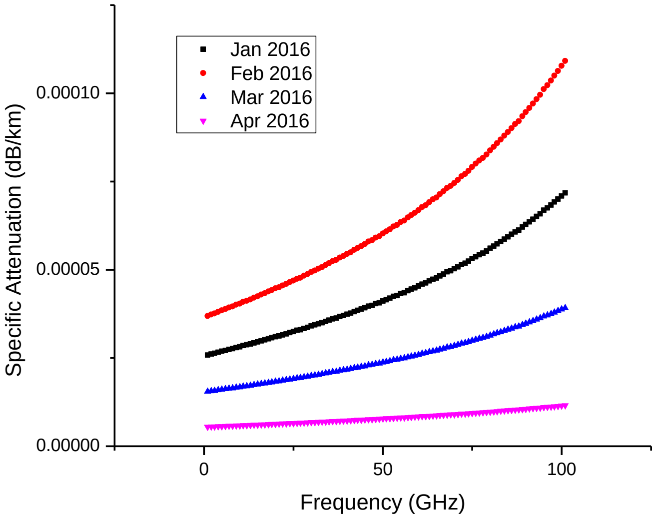

Figure 5.13: Graph of Rain Attenuation versus Frequency from August - October 2015

Figures 5.12 and 5.13 illustrate the graph of graph of attenuation due to rain against frequency from August 2015 to December, 2015 and then January, 2016 to April, 2016 respectively. The rain attenuation was calculated using the ITU-R model. The attenuation due to rain increased with increasing frequencies. As can be seen in Figure 5.12, the month of November 2015 had the highest attenuation values whiles August 2015 had the lowest attenuation values.

From Figure 5.13, it was observed that April 2016 had the highest attenuation values whiles February 2016 had the lowest attenuation values. Figures 5.12 and 5.13 correlated with bi-modal rainy seasons in southern Ghana: April through June and September through November**.**

5.2.3 Additional Data Analysis (Axim)

On account of the fact that relative humidity data was measured using the Davis weatherstation, work was done to determine any correlation between the visibility and rain rate and also between visibility and relative humidity. Analysis done on these data sets are shown in the graphs shown in Figures 5.14 to 5.16b. This analysis was done using measurements obtained in Axim for all weather (harmattan and rainfall) and all-day (morning and night) for days in 2016.

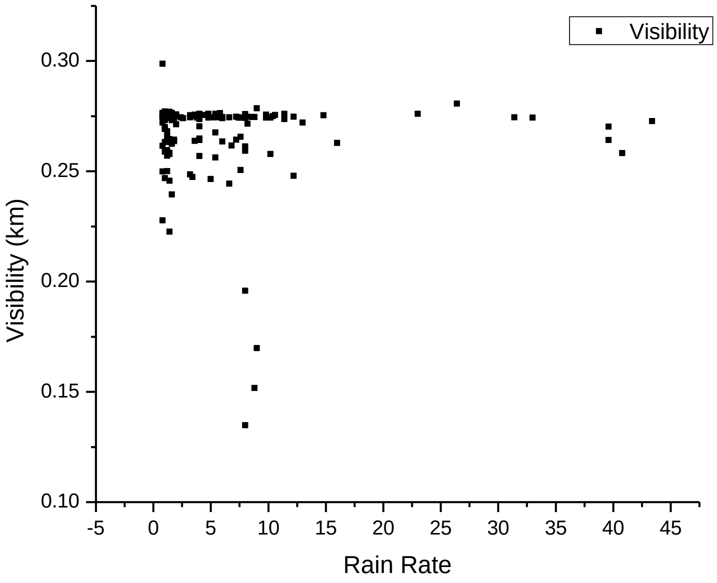

Figure 5.14: Graph of Visibility versus Rain Rate in Axim

Figure 5.14 demonstrated a graph of visibility against rain rate in Axim. It was observed that there was no obvious correlation was observed between the visibility and rain rate.

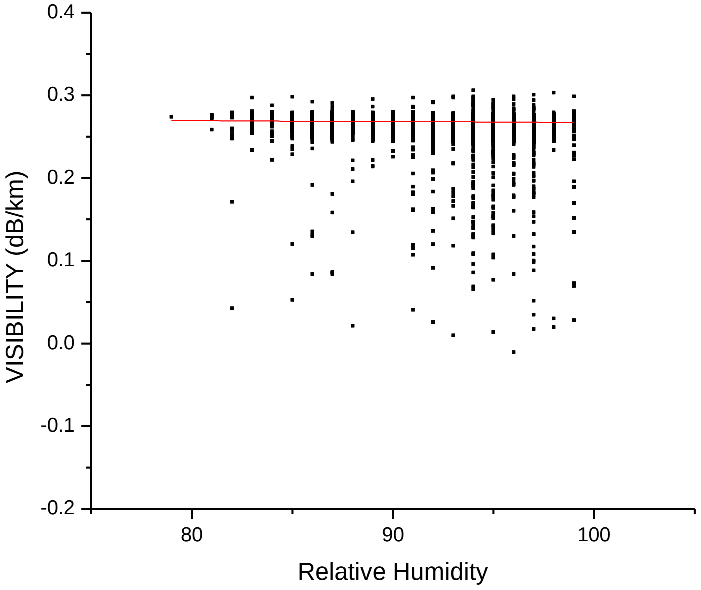

Figure 5.15: Graph of Visibility versus Relative Humidity (All-Day, All Weather) in Axim

Figure 5.15 demonstrated a relation between visibility against relative humidity with measurements from Axim. A cluster was obtained showing no relation between the two parameters. Furthermore, analysis was done using xyz plots for visibility, relative humidity and temperature to determine and further relationship between visibility and other weather parameters such as temperature.

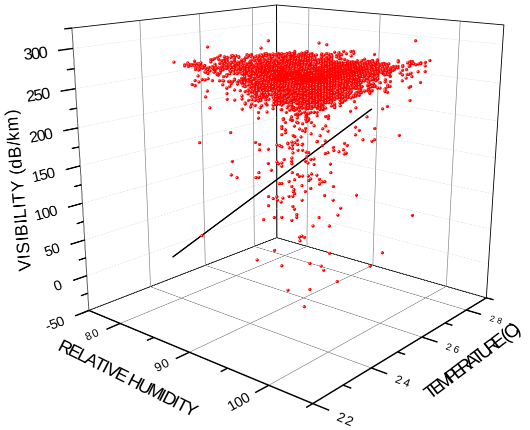

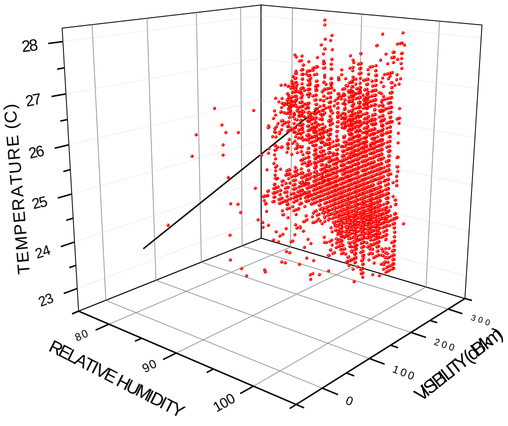

Figure 5.16a: XYZ Graph of Visibility against Relative Humidity and Temperature

Figure 5.16b: XYZ Graph of Temperature against Visibility and Relative Humidity

Figure 5.16a and 5.16b shows xyz plots of visibility with relative humidity and temperature. Figure 5.16a illustrated a graph of visibility against relative humidity and temperature whiles Figure 5.16b illustrated a graph of temperature against relative humidity and visibility. In both plots, it was observed that the relative humidity and temperature both affect the visibility. No obvious correlation was obtained between the three variables.

5.3 Tamale Measurements

5.3.1 Harmattan Dust Results

Visibility readings were recorded in Tamale for the month of December, 2016 and 2017. The signal attenuation due to harmattan dust for the different frequency bands was calculated.

During the course of measurements, visibility values recorded were relatively low during 2016 in the Tamale during the harmattan season. Visibility was measured using the Campbell Scientific Visibility Sensor. For most of the events, the low values of visibilities ranged 0.225 km to 0.262 km.

The specific attenuation as a result of harmattan dust was calculated for the averaged visibility values recorded in Tamale. Figure 5.17 – Figure 5.23 shows the graphs of the signal attenuation against frequency bands in the range of 10 - 100 GHz.

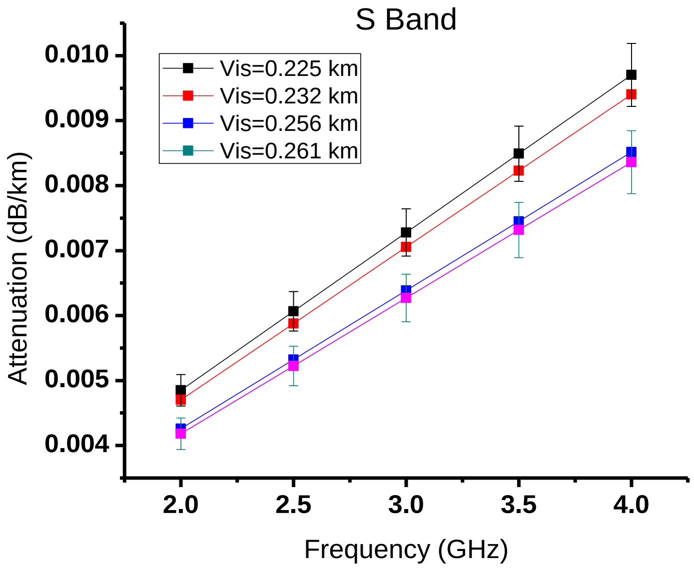

Figure 5.17: Signal Attenuation versus Frequency at S-Band for Different Visibilities in Tamale

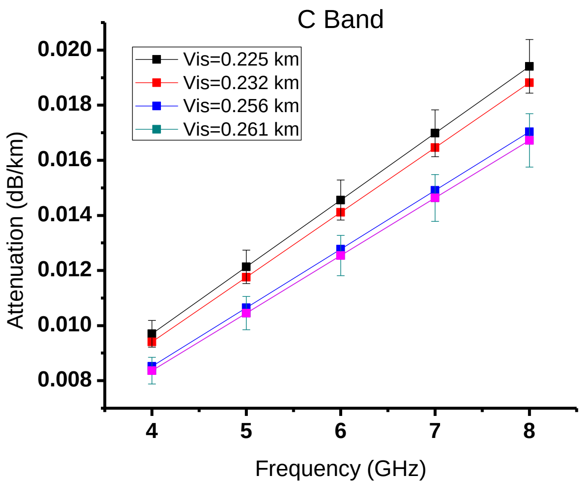

Figure 5.18: Signal Attenuation versus Frequency at C-Band for Different Visibilities in Tamale

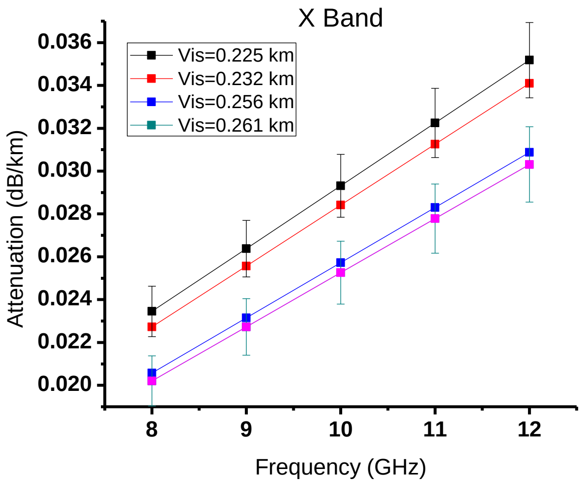

Figure 5.19: Signal Attenuation versus Frequency at X-Band for Different Visibilities in Tamale

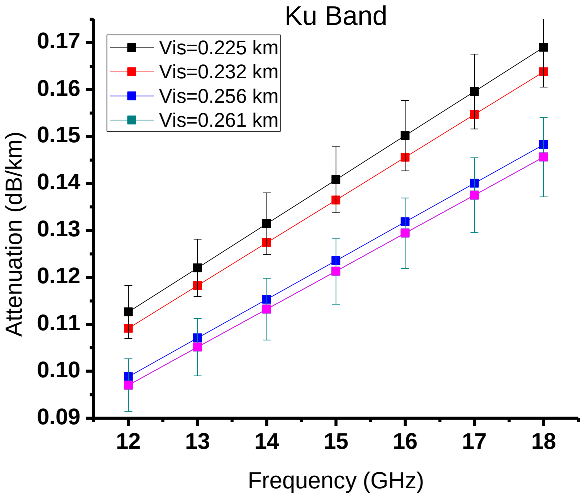

Figure 5.20: Signal Attenuation versus Frequency at Ku-Band for Different Visibilities in Tamale

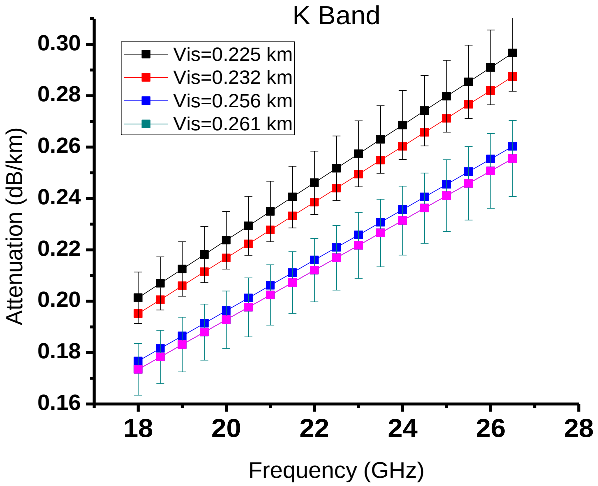

Figure 5.21: Signal Attenuation versus Frequency at K-Band for Different Visibilities in Tamale

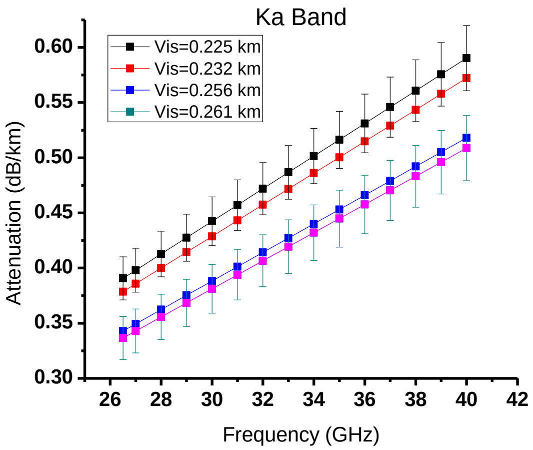

Figure 5.22: Signal Attenuation versus Frequency at Ka-Band for Different Visibilities in Tamale

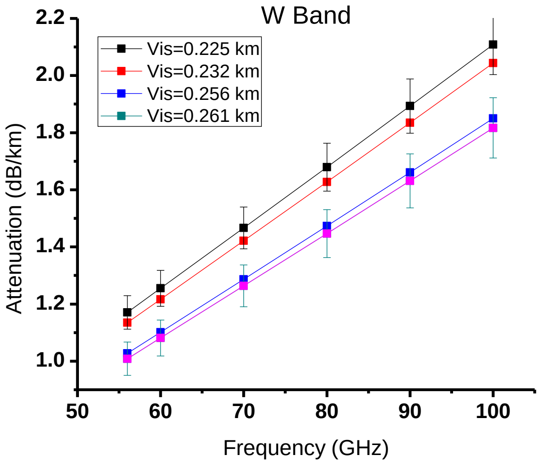

Figure 5.23: Signal Attenuation versus Frequency at W-Band for Different Visibilities in Tamale

As observed in the Axim data, Figures 5.17 to Figure 5.23 show the signal attenuation against the different frequency band for different visibilities in Tamale. Figure 5.17 showed that for the S-band which demonstrated the attenuation values increasing with increasing frequency. The same trend run through for the different frequency bands as can be seen in figures 5.18 to 5.23, that is, from the C-band to the W- band.

For Tamale, the different visibilities showed different attenuation values with the attenuation values reaching the highest values for the least visibilities and vice versa. In addition, the attenuation values increased with the increasing frequency band ranges.

Figures 5.24 to 5.27 show the calculated attenuation using the Zain Elabdin model for the average visibility values measured (0.225 km, 0.232 km, 0.256 km, 0.261 km) at frequencies ranging from 10 GHz to 100 GHz for varying dust particle sizes. This analysis follows from the analysis done in Axim.

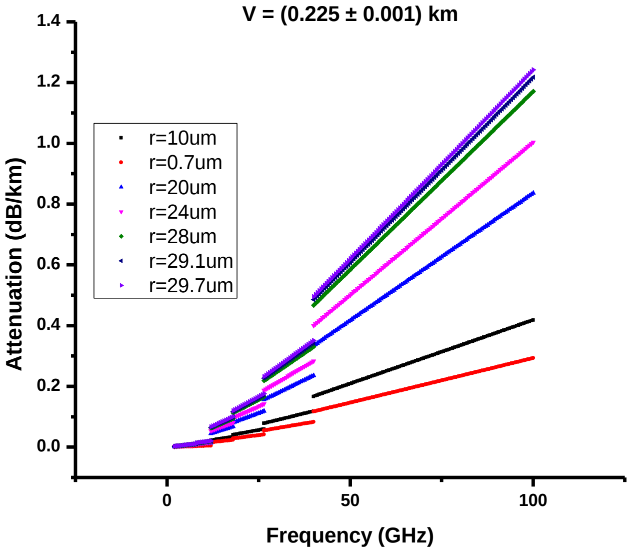

Figure 5.24: Signal Attenuation due to harmattan against Frequency at Vis = 225.482m for different radii

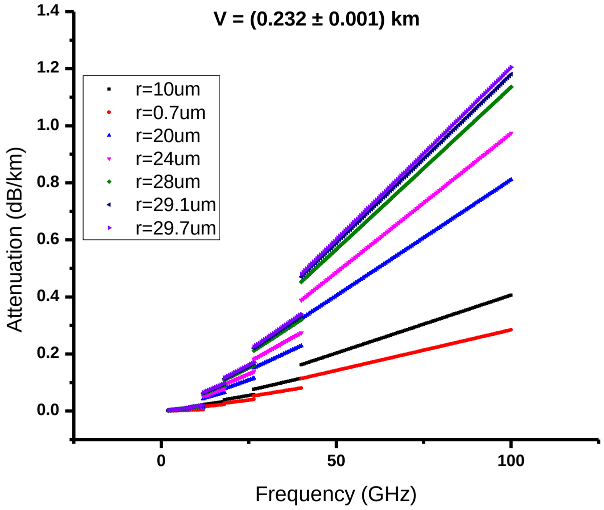

Figure 5.25: Signal Attenuation due to harmattan against Frequency for Vis = 232.64m at different radii

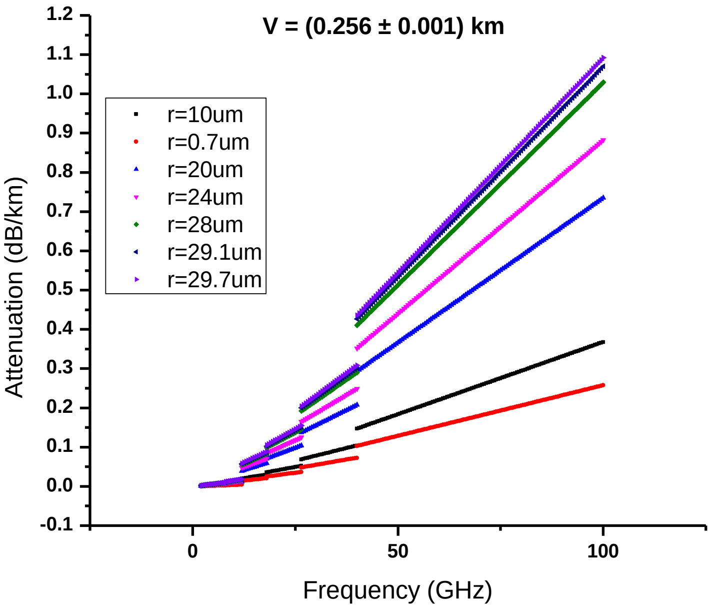

Figure 5.26: Signal Attenuation due to harmattan against Frequency for Vis = 256.95m at different radii

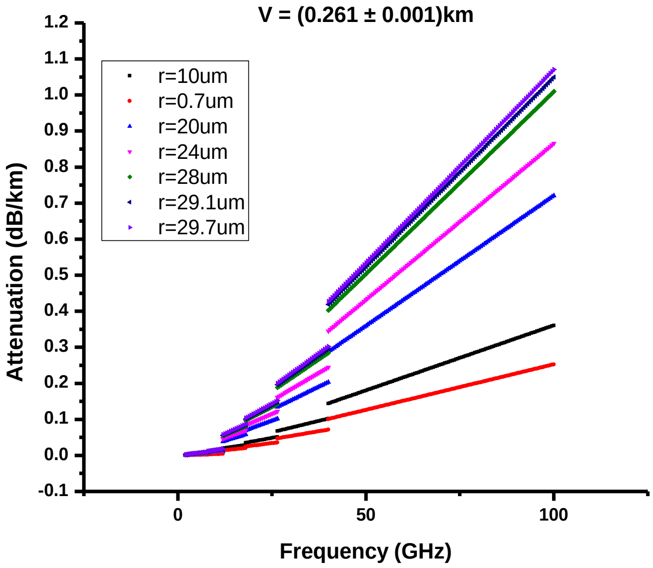

Figure 5.27: Signal Attenuation due to harmattan against Frequency at Vis = 261.70m for different radii

It was found that the attenuation remained within the same range (~ 0.1 dB/km to ~1.2 dB/km) for all the four varying average visibilities across all the different particle sizes. The attenuation values in Tamale were comparatively lesser than those in Axim.

It was observed that the signal attenuation increased as the radius size increased for frequencies from 10 – 100 GHz. Some discontinuities were observed in the trend. This was as a result of the transition between different frequency bands. The graph obtained was as expected from the equation since frequency is directly proportional to attenuation.

5.3.2 Rain Rate Results

Figure 5.28 shows the graph of rain attenuation against the frequency from April, 2016 to June, 2016. The rain attenuation was calculated using the ITU-R model. As can be seen in Figure 5.28, the month of June had the highest attenuation levels with its higher peak values at about 0.000425 dB/km while May had the lower attenuations with dip attenuation values of about 0.00008 dB/km.

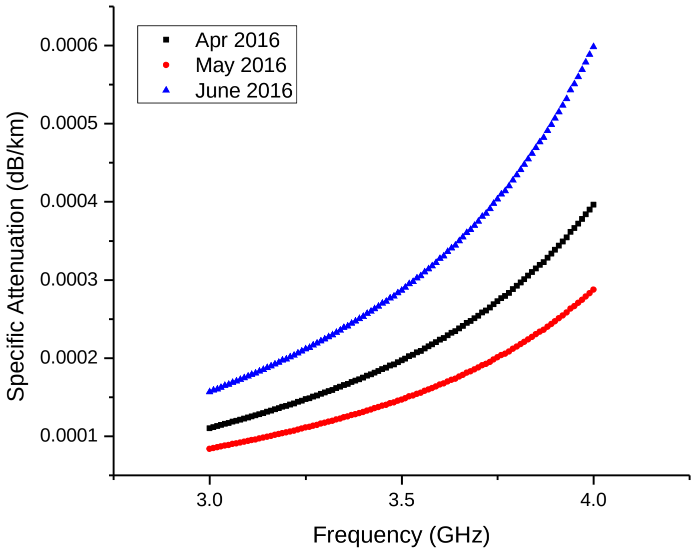

Figure 5.28: Graph of Rain Attenuation versus Frequency from April -June 2016

5.3.3 Additional Data Analysis (Tamale)

On account of the fact that relative humidity data was measured using the Davis weatherstation, work was done to determine any correlation between the visibility and rain rate and also between visibility and relative humidity. Analysis done on these data sets are shown in the graphs shown in Figures 5.29 to 5.30b. This analysis was done using measurements obtained in Tamale for all weather (harmattan and rainfall) and all-day (morning and night) for days in 2016.

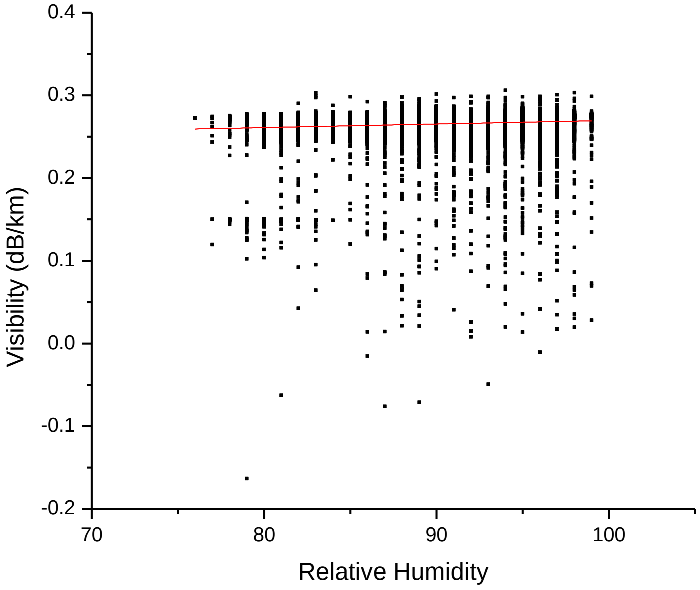

Figure 5.29: Graph of Visibility versus Relative Humidity (All-Day, All Weather) for Tamale

Figure 5.29 demonstrates a relation between visibility against relative humidity with measurements from Tamale. A cluster was obtained showing no relation between the two parameters. Additionally, analysis was done using xyz plots for visibility, relative humidity and temperature to determine any further relationship between visibility and other weather parameters such as temperature.

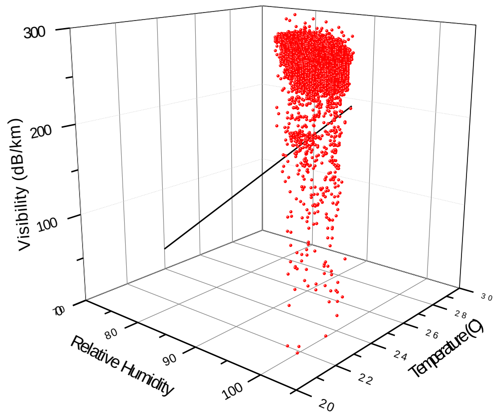

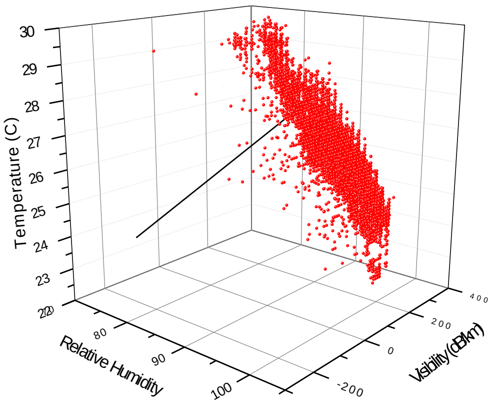

Figure 5.30a: XYZ Graph of Visibility against Relative Humidity and Temperature

Figure 5.30b: XYZ Graph of Temperature against Visibility and Relative Humidity

Figure 5.30a and 5.30b shows xyz plots of visibility with relative humidity and temperature. Figure 5.30a illustrates a graph of visibility against relative humidity and temperature whiles Figure 5.30b illustrates a graph of temperature against relative humidity and visibility. From the xyz plots shown in Figures 5.30a and 5.30b, it can be observed that changes in temperature values as well as relative humidity values have an effect on visibility. No obvious correlation was obtained between the three variables.

5.4 Signal Attenuation due to Dust for Different Radii

Using the Zain model, the attenuation coefficients of different particle radius sizes were calculated at a frequency of 40GHz using information about the different mean radii from Elsheikh *et al* (2010) and the radii used for this research obtained from different papers. The radii (a_e) used were 29.7µm, 24 µm, 20 µm, 10 µm and 0.7 µm. The radius used for this research was 10 µm whiles 0.7 µm was obtained from Hughes (2015) paper. The remaining radii were from the Elsheikh *et al* (2010) paper. Figures 5.31 and 5.32 showed the attenuation against visibility for the different particle sizes. This was done in both Tamale and Axim.

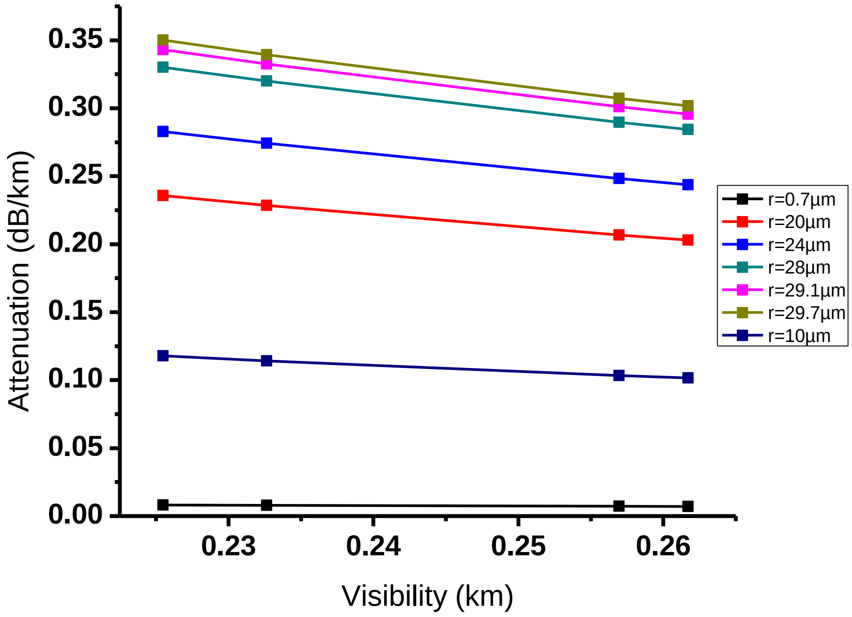

Figure 5.31: Signal Attenuation due to harmattan against Visibility at 40 GHz for different radii in Tamale

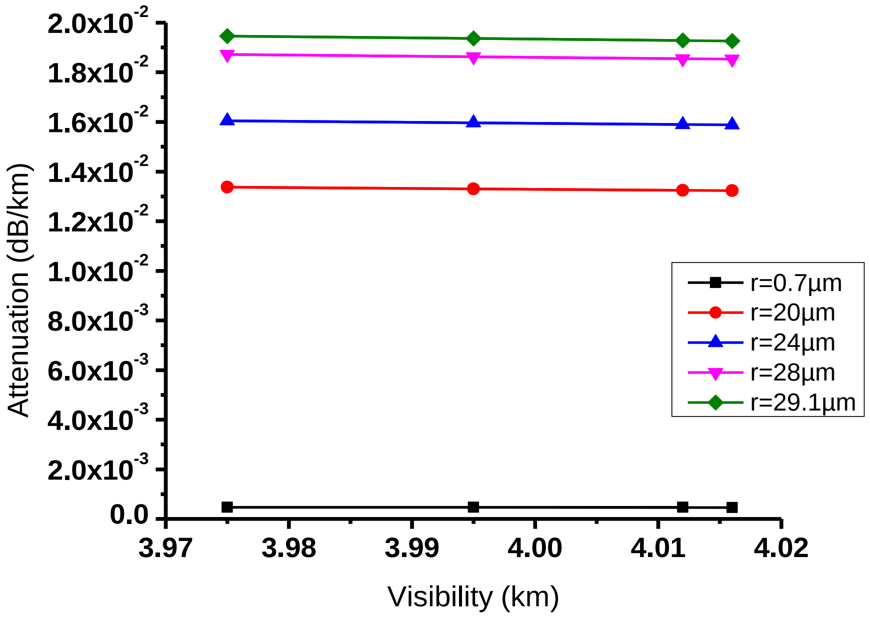

Figure 5.32: Signal Attenuation due to harmattan against Visibility at 40 GHz for different radii in Axim

For both Axim and Tamale, it was observed that attenuation values increased with increasing particle size. For Tamale (Figure 5.31), it was observed that the largest particle size radius (a_e = 29.7µm) reached the highest attenuation values calculated at frequency 40GHz at the different visibilities, whereas the smallest particle radius (a_e = 0.7µm), attained the lowest attenuation values which was calculated at frequency 40GHz. Similarly for Axim, Figure 5.32 showed that the largest particle size radius (a_e = 29.7µm) reached the highest attenuation values calculated at frequency of 40GHz at the different visibilities, while the lowest attenuation values which was calculated at frequency 40GHz were obtained for the smallest particle radius (a_e = 0.7µm).

Also, it was observed from Figure 5.31 that the signal attenuation graphs showed a very slight decline for the lower radius sizes (a_e = 0.7µm and a_e = 10µm) but had a more gradual decline for the remaining larger radii (a_e = 20µm, 24µm and 29.7µm). On the other hand, Figure 5.32 indicated that all the signal attenuation graphs maintained a a very slight decline for the respective visibilities.

5.4.1 Comparison Between The Measured And Prediction Models

Attenuation values were calculated for different values of visibility at 40 GHz in Axim and Tamale. This is shown in Table 5.2 below:

Visibility(km)	**Att. from Elsheikh paper**	**Calculated Attenuation (My Study)**
0.225482	0.141377426	0.117827039
0.232641	0.140886547	0.1142012
0.256953	0.139226214	0.103395704
0.261701	0.138903168	0.101519749

Table 5.2: Result of Measurements and Calculations of Signal Attenuation Due To Harmattan at 40 GHz in Tamale

Figure 5.33 represents a comparative analysis between attenuation values obtained from the aforementioned Elsheikh *et al* (2010) paper and the calculated attenuation values at 40GHz with visibility values from Tamale. Both sets of attenuation values were obtained using the Zain Elabdin model at a frequency of 40GHz.

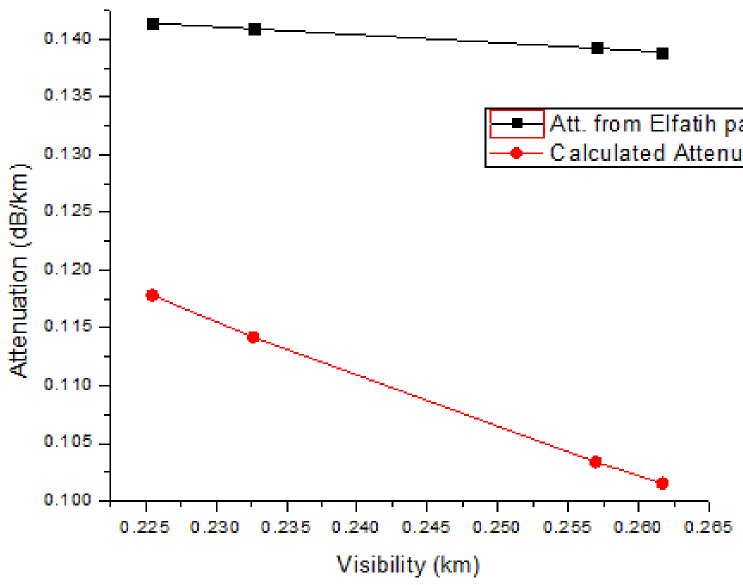

Figure 5.33: Result of Measurements and Calculations of Signal Attenuation Due To Harmattan Dust at 40GHz

Comparatively from Figure 5.33, the attenuation recorded from the Elsheikh paper was much higher with a maximum and minimum attenuation value of 0.1414 dB/km and 0.1389 dB/km respectively as compared with the maximum and minimum calculated attenuation value of 0.1178 dB/km and 0.1015dB/km respectively obtained from the measured visibilities in Axim.

The graph showed a steeper decline for the calculated values than the more gradual decline seen for the Elsheikh paper. This implies there is a lower visibility due to less dust particles in the atmosphere in Tamale than in Sudan (where this work was done).

The values of the slope and the intercept for the attenuation obtained from the Elsheikh paper are (–0.06831 ± 3.66378 x 10^{-5}) dB/km and (0.15678 ± 8.9646 x 10^{-6}) dB/km respectively. Similarly, the slope and intercept for the attenuation obtained from the calculated attenuation obtained from this work are (-0.44887 ± 0.00788) dB/km and (0.21885 ± 0.00193) dB/km respectively.

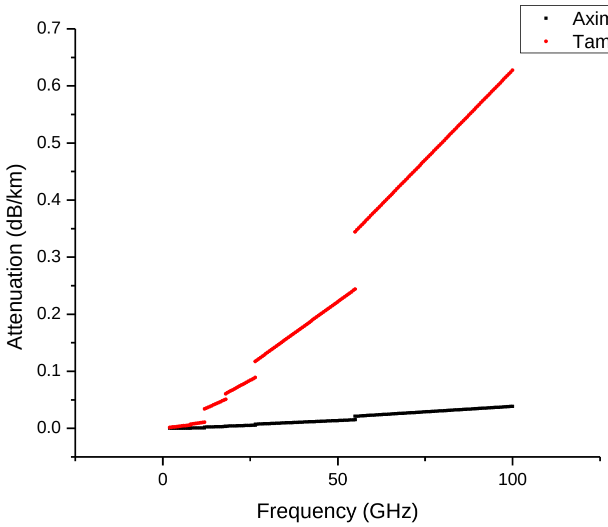

Figure 5.34: Comparison of Calculated Signal Attenuation Due To Harmattan Dust at Different Frequencies in Axim and Tamale

Figure 5.34 shows a graph of attenuation due to harmattan dust against frequency. The attenuation values were calculated using the Zain Elabdin model. In Figure 5.34, the signal attenuation due to harmattan was calculated for frequencies ranging from 10 – 100 GHz for both Tamale and Axim.

The signal attenuation due to harmattan increased with increasing frequencies for both locations. It was observed that Tamale had the higher attenuation values. Axim showed relatively low attenuation values from frequencies of 10 GHz to 100 GHz and ranged from 0.00009 dB/km to 0.03841 dB/km whiles signal attenuation values for Tamale increased from 0.00146 dB/km to its maximum value of 0.6272 dB/km. This graph shows that attenuation due to dust was more prevalent in the Tamale than in Axim.

CHAPTER SIX

CONCLUSIONS AND RECOMMENDATIONS

6.1 Summary of Experiment

In this study, visibility data were measured at two study sites in Axim and Tamale. Additionally, rainfall and other meteorological data were collected in Axim and Tamale.

The recorded visibility data was then used to calculate the signal attenuation due to harmattan dust using the Zain Elabdin model. Similarly, the rainfall rate data was used to determine the rain attenuation using the ITU-R model. Also, there were comparisons made between calculated results using the Zain model attenuation model and the results from some chosen papers. Finally, work was done to determine any correlation between the visibility and rain rate and also between visibility and relative humidity. This was done for both Axim and Tamale. Measurements used for the analysis were obtained for all weather (harmattan and rainfall) and all-day (morning and night) for days in 2016.

6.2 Key Results

In summary, the overall result of this experiment was that both harmattan dust and rainfall have a significant impact on signal attenuation in parts of Ghana. The impact of the attenuation due to harmattan dust was much more evident in Tamale whiles rain attenuation was more evident in Axim. Additionally, on analysing attenuation due to harmattan dust for the different frequency bands from 10 – 100 GHz, it was observed that the signal attenuation increased with the increasing frequency bands for both Axim and Tamale. For the Axim site, the attenuation values were approximately the same for all the visibilities. On the contrary for Tamale, the different visibilities produced different attenuation values with the attenuation values reaching the highest values for the least visibilities and vice versa.

The attenuation was calculated using the Zain Elabdin model for the four average visibility values at frequencies ranging from 10 GHz to 100 GHz using different values of particle radius obtained from the Elsheikh *et al* (2010) paper. It was observed that the signal attenuation remained within the same range of 0.1 dB/km to 0.12 dB/km for all the four varying average visibilities across all the different particle sizes for Tamale whiles attenuation in Axim remained was in the range of 0.01 dB/km to 0.07 dB/km for all the four varying average visibilities across all the different particle sizes.

It was observed that the signal attenuation increased as the radius size increased for frequencies from 10 – 100 GHz. Some discontinuities were observed in the trend. This was as a result of the transition between different frequency bands. The graph obtained was as expected from the equation since frequency is directly proportional to attenuation.

Furthermore, as shown in the ITU-R rain attenuation model, attenuation values were highest with high rainfall rates while the lowest attenuation values corresponded to the lowest rainfall rates.

Using the Zain model, the attenuation coefficients of different particle radius sizes were calculated at a frequency of 40GHz using information about the different mean radii from Elsheikh *et al* (2010), the radius used for this research and radius obtained from Hughes (2015) paper. The radii (a_e) used were 29.7µm, 24 µm, 20 µm, 10 µm and 0.7 µm. The radius used for this research was 10 µm. This was done for both Axim and Tamale.

For both Axim and Tamale, it was observed that the largest particle size radius (a_e = 29.7µm) reached the highest attenuation values calculated at frequency 40GHz for the different visibilities, whereas the smallest particle radius (a_e = 0.7µm), attained the lowest attenuation values which was calculated at frequency 40GHz. For Tamale, it was noted that the signal attenuation showed very slight decline for the lower radius sizes (a_e = 0.7µm and a_e = 10µm) but showed a more gradual decline for the remaining larger radii (a_e = 20µm, 24µm and 29.7µm). On the other hand, the analysis indicated that all the signal attenuation in Axim maintained a relatively constant plot at the respective visibilities.

The signal attenuation due to harmattan dust was calculated for frequencies ranging from 10 – 100 GHz for both Tamale and Axim. The signal attenuation due to harmattan dust increased with increasing frequencies for both locations. Upon comparison, it was observed that Tamale had the higher attenuation values.

Axim showed relatively low attenuation values from frequencies of 10 GHz to 100 GHz and ranged from 0.00009 dB/km to 0.03841 dB/km whiles signal attenuation values for Tamale increased from 0.00146 dB/km to its maximum value of 0.6272 dB/km. This graph shows that attenuation due to dust was more prevalent in the Tamale than in Axim.

Finally, a comparative analysis between the attenuation values obtained from the aforementioned Elsheikh *et al* paper and the calculated attenuation values against the visibility measurements recorded in this research. Both sets of attenuation values were obtained using the Zain Elabdin model at a frequency of 40GHz. The attenuation recorded from the Elsheikh *et al* paper was much higher than the attenuation values obtained from the calculated attenuation values.

Finally, analysis work done to obtain any correlation between visibility and rain rate and visibility and relative humidity showed no relation between the two parameters in both cases. Further analysis using xyz plots of visibility with relative humidity and temperature showed that changes in temperature values as well as relative humidity values have an effect on visibility. No obvious correlation was obtained between the three variables.

In summary, the conclusions of this research work are as follows:

- The two models used for calculating the attenuation due to harmattan dust and rain are the Zain Elabdin Model and the ITU-R Specific Attenuation Model for Rain respectively. It has been successfully shown that using visibility and rain rate, these two models can predict attenuation in Ghana.

- A study by Elfatih *et al* (2013) obtained attenuation due to dust storm in Sudan. It has been shown that the attenuation measured from dust particles in Tamale is much smaller than the attenuation values obtained from the Elfatih paper. Clearly the origin, size and concentration of the dust is important.
- As expected, the impact of the attenuation due to harmattan dust was significantly evident in Tamale while that of rain attenuation was more evident in Axim.
- Contrary to our expectation, no systematic correlation was obtained between visibility and rain rate.
- Additionally, no observable correlation was obtained between the visibility and relative humidity.

6.3 Further Research and Recommendation

It has been noted that RF wave propagation above in the atmosphere is affected by the various weather conditions. While this study has clearly shown the impact that harmattan dust and rainfall has on microwave attenuation in parts of Ghana, it is recommended that this experiment be repeated over a much longer time frame, with a wider range of environmental conditions, and over a wider set of frequencies, varying particle sizes and measured signal strength.

In my study, it was not possible to measure particle size. It will be interesting for further work to be done to observe the effects of varying particle sizes on attenuation. Additionally, the availability of measured signal strength would have made this study easier. It is therefore recommended that further work be done using measured signal strength. Finally, further research on the role of relative humidity on attenuation is recommended.

All of the above recommendations would ultimately lead to a better understanding of how various weather conditions affect microwave attenuation.

REFERENCES

Atkins R. (1991), *Radio Propagation by Tropospheric Scattering, A reliable propagation mode for working VHF/UHF/microwave DX. Communications Quarterly*, pp. 119-127.

Bilford I. H. and Gillette D. A. (1971), *Application of the lognormal frequency distribution to the chemical composition and size distribution of naturally occurring atmospheric aerosols,* Water Air & Soil Pollut., vol. 1, pp. 106-114.

Brussaard G. and Watson P. A. (1995) *Atmospheric modelling and millimetre wave propagation*, Chapman & Hall.

Cachorro V. E. (2001) *New Improvements For Mie Scattering Calculations*, eprintarXiv:physics/0103052

Collin, R. E. (1985) *Antenna and Radiowave Propagation*, McGraw-Hill.

Clark I. and Abbott J. (2012), *White Paper: The Case for Forward Scatter Sensors for IRVR*, Aeronautical & General Instruments Limited

Chu T. S. (1979), *Effects of sandstorms on microwave propagation*, Bell Sys. Tech. J. v. 58, no. 2.

Elfadil N., Nadir Z., Salam A. and Rao J., (2005) *Microwave Attenuation Studies Due To Rain For Communication Links Operating In Malaysia*, Georgian Electronic Scientific Journal: Computer Science and Telecommunications| No.1 (5).

Elabdin Z., Islam R., Khalifa O. O., Essam H. A. R. and Salami M. J. E. (2008) *Development of Mathematical Model for the Prediction of Microwave Signal Attenuation due to Duststorm*, Proceedings of the International Conference on Computer and Communication Engineering, 2008 May 13-15, 2008 Kuala Lumpur, Malaysia.

Elabdin Z., Islam M.R., Khalifa O. O. and Raouf H. E. A. (2009) *Mathematical Model for the Prediction of Microwave Signal Attenuation Due To Dust storms*, Progress in electromagnetic research M, Vol. 6, pp. 139-153.

Elsheikh E. A. A., Islam M. R., Alam A.H.M.Z., Ismail A. F., Al-Khateeb K. and Elabdin Z.(2010). *The Effect of Particle Size Distributions on Dust Storm Attenuation Prediction for Microwave Propagation*, International Conference on Computer and Communication Engineering.

Eyo O. E., Menkiti A. I. and Udo S. O. (2003) *Microwave Signal Attenuation in Harmattan Weather along Calabar-Akamkpa Line-of-Sight Link,* Turkish Journal of Physics 27, 153-160. Mark J. W. and Zhuang W. (2005) *Wireless Communications and Networking*, New Delhi: PHI.

Folland, C.K., Karl T.R. and Vinnikov K.Y. (1990). *Observed climate variations and change. In Climate Change: The IPCC Scientific Assessment*, Prepared for the Intergovernmental Panel on Climate Change by Working Group I. Cambridge University Press, Cambridge, pp. 195-238.

Freeman R. L. (2007) *Radio System Design for Telecommunications*, Third Edition, John Wiley & Sons, 978-0-47175-713-9 New York.

Freeman R. L., (2008) *Telecommunications Transmissions Handbook*, John Wiley and Sons Inc. Publications, fourth edition, pp. 553-572.

Ghasemi A., Abedi A. and Ghasemi F. (2012) *Propagation Engineering in Wireless Communications,* XVII, 434, pp. 176.

Ghasemi A., Abedi A. and Ghasemi F. (2013), *Propagation Engineering in Radio Links Design*, pp. 125-210.

Ghobrial S. I. and Sharief S. M. (1987), *Microwave attenuation and cross polarization in dust storms*, IEEE Trans. Antennas Propagat., v. AP-35, pp. 418–425.

Ghobrial S. I. (1980), *The effect of sand storms on microwave propagation*, Proc. Nat. Telecommun. Conf., Houston, TX. vol. 2, Proc. No. CH1539-6/80/0000-0216, pp. 43.5.1-43.5.4.

Goldhirsh J. (2001), *Attenuation and backscatter from a derived two-dimensional duststorm model*, IEEE Transactions on Antennas and Propagation, vol. 49, no. 12, pp. 1703-1711, doi: 10.1109/8.982449.

Grams G. W., Bilford I. H., Gillette D. A. and Russell P. B. (1974), *Complex index of refraction of airborne soil particles,* J. Appl. Meteoroi, vol. 13, pp. 459-471.

Griffiths, D. J. (1999), *Introduction to electrodynamics*. Prentice Hall.

Gurung S. and Zhao J., *Attenuation of Microwave Signal and its Impacts on Communication System.*

Haddad S., Salman M. J. H. and Jha R. K. (1983), *Effects of dust/sand storms on some aspects of microwave propagation*", Proc. Ursi Comm. F1983 Symp., pp. 153-162.

Hall, M. P. M., Barclay L. W. and Hewitt M.T. (1996), *Propagation of Radiowaves*, chap. 1–4, IEE Press, London.

Hayward, D. and Oguntoyinbo, J. (1987). *The Climatology of West Africa*. Hutchinso, London, pp. 271.

Hughes, A., (2015), *Characterization and Source Apportionment of Airborne Particulate Matter in some Urban Neighborhoods of Accra, Ghana.*

Ishimaru A. (1997). *Wave Propagation and Scattering in random media* IEEE, N.Y.

Ishimaru A. (1997). *Wave Propagation and Scattering in Random Media, Vol. 2, Multiple Scattering, Turbulence, Rough Surfaces and Remote Sensing*, IEEE Press, Piscataway.

Islam R. and Tharek A. R. (1999) *Propagation Study of Microwave Signals Based on Rain Attenuation Data at 26 GHz and 38 GHz measured in Malaysia*, IEEE Transactions on Communications, pp. 602.

Islam R., Abdulrahman Y. A. and Rahman T. A.(2012) *An improved ITU-R rain attenuation prediction model over terrestrial microwave links in tropical region,* EURASIP Journal on Wireless Communications and Networking 2012:189

ITU-R (2001), *Propagation prediction techniques and data required for the design of terrestrial line-of-sight systems,* Recommend. 530-10, ITU-R P Ser., pp. 271–295, Int. Telecommun. Union, Geneva.

Kadi M, Njau LN, Mwikya J. and Kamga A. (2011). *The State of Climate Information Services for Agriculture and Food Security in East African Countries*. CCAFS Working Paper No. 5. Copenhagen, Denmark.

Kakane V. C. K. (1998), *Measurement of Evapotranspirationand the Investigation of its Relation with NDVI*

Kumari A. (2017). *Analysis of Atmospheric Scattering from Digital Images using Temporal Polarized Vision*, International Research Journal of Engineering and Technology (IRJET) Volume 04

Lee W. C. Y. (1995) *Mobile Cellular Telecommunications Analog and Digital Systems*, Mc-Graw-Hill, Inc, Second Edition, Chapter 12, pp. 365.

Mark J. W. and Zhuang W. (2005) *Wireless Communications and Networking*, New Delhi: PHI.

McSweeney, C., Lizcano, G., New, M. and Lu, X. (2010) The UNDP Climate Change Country Profiles.

Mohammed B. A. (2010) *Prediction of Microwave Attenuation Due to Dust Storms over Iraq*, AL- Mustansiriya J. Sci Vol. 21, No 7.

Moupfouma, F. (1984), *Improvement of rain attenuation prediction method for terrestrial microwave links*, IEEE Trans. Antennas Propag., 32(12), pp. 1368–1372.

Muench Stuart H. et al. (1974), *Development and Calibration of the Forward Scatter Visibility Meter*, Air Force Cambridge Research Laboratories L. G. Hanscom Field, Massachusetts.

Nkrumah, F., Brown K. N. A., Adukpo D. C., Owusu K., Quagriane K. A., Owusu A. and Gutowski W. (2014), *Rainfall Variability over Ghana: Model versus Rain Gauge Observation*, International Journal of Geosciences, 5, pp. 673-683. http://dx.doi.org/10.4236/ijg.2014.57060

Oguchi T. (1983), *Electromagnetic wave propagation and scattering in rain and other hydrometeors*, Proceedings of the IEEE, vol. 71, no. 9, pp. 1029-1078.

Olsen L., Roderic & Rogers, David and B. Hodge, Daniel. (1978). *The aRb Relation in the Calculation of Rain Attenuation. Antennas and Propagation*, IEEE Transactions.

Ojo J. S., Ajewole M. O. and Sarkar S. K. (2008) *Rain Rate And Rain Attenuation Prediction For Satellite Communication In Ku And Ka Bands Over Nigeria*, Progress In Electromagnetics Research B, Vol. 5, pp. 207–223.

Owusu, K. and Waylen, P.R. (2013), *The Changing Rainy Season Climatology of Mid-Ghana*. Theoretical and Applied Climatology, 112, pp. 419-430.

Patterson E. M. and Gillette D. A. (1977), *Commonalities in measured size distribution for aerosols having a soil-derived component*, J. Geophy. Res, vol. 82, pp. 2074-2082.

Pozar, D. M. (1988), *Microwave Engineering*, 2nd ed., chap. 12, John Wiley, New York.

Rappaport T. S. (2002) *Wireless Communications: Principles and Practice*, 2nd ed. Singapore: Pearson Education, Inc.

Roda G. (1988), *Troposcatter Radio Links*, Artech House, Norwood, MA, pp. 43.

Row D. R., Nouh M. A., Dowalia A. L, Mansour K. H and M. E. (1985), *Indoor-outdoor relationship of suspended particulate matter in Riyadh Saudi Arabia*, J. Air Pollut. Control Assoc, vol. 35, no. 1, pp. 24-26.

Ruike Y., Zhensen W. and Jinguang Y. (2003), *The Study Of MMW and MW Attenuation Considering Multiple Scattering Effect in Sand and Dust Storms at Slant Paths*, International Journal of Infrared and Millimeter Waves, Vol. 24, No. 8.

Schilling D. L. and Taub H. (1986), *Principles of Communications Systems* 2d ed., McGraw Hill Higher Education.

Shoewu, O and Edeko F.O. (2011) *Microwave signal attenuation at 7.2GHz in Rain and Harmattan Weather,* American Journal of Scientific and Industrial Research, Science Huβ.

Seybold John S. (2005), *Introduction to RF Propagation*, John Wiley & Sons, Inc.

Uzma S., Laeeq A., Gulistan R. (2011) *Microwave Attenuation and Prediction of Rain Outage for Wireless Networks in Pakistan's Tropical Region,* Hindawi Publishing Corporation International Journal of Microwave Science and Technology Volume 2011, Article ID 714927.

Vishvakarma B.R. Rai C.S. (1993). *Limitations of Rayleigh scattering in The Prediction of Millimeter Wave Attenuation in Sand and Dust Storms*, Geoscience and Remote Sensing Symposium, IEEE Intr.